CHARACTERIZATION OF
BARIUM TITANATE AS AN
OPTICAL AMPLIFIER

DISSERTATION
George A. Vogel

AFIT/DS/ENG/90D-3
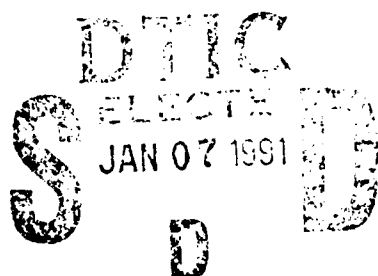
DEPARTMENT OF THE AIR FORCE
AIR UNIVERSITY

AIR FORCE INSTITUTE OF TECHNOLOGY

Wright-Patterson Air Force Base, Ohio

91 1 43 101

AFIT/DS/ENG/90D-3

CHARACTERIZATION OF
BARIUM TITANATE AS AN
OPTICAL AMPLIFIER

DISSERTATION

George A. Vogel

AFIT/DS/ENG/90D-3

CHARACTERIZATION OF BARIUM TITANATE

AS AN OPTICAL AMPLIFIER

DISSERTATION

Presented to the Faculty of the School of Engineering

of the Air Force Institute of Technology

Air University

In Partial Fulfillment of the

Requirements for the Degree of

Docter of Philosophy

George A. Vogel, B.S.,M.S.

A-1

December,1990

CHARACTERIZATION OF BARIUM TITANATE
AS AN OPTICAL AMPLIFIER

George A. Vogel, B.S.,M.S.

Approved:

(signature)	26 Nov 90
(signature)	26 Nov 90
(signature)	26 Nov 90

(signature) 3 Dec. 90

J. S. Przemieniecki

Institute Senior Dean

Preface

The purpose of this effort was to determine the practical limits within which two-beam coupling in Barium Titanate could be used as an optical amplifier. A significant amount of work had already been performed in understanding the two-beam gain process to the point of being able to characterize a particular crystal. Very little had been done, however, with analyzing the amplified noise process (commonly known as beam fanning) and trying to control its level. The optimization of the optical amplifier is the result of trading off gain and dynamic range, with the latter parameter determined by the saturated output level and the amplified noise. This dissertation provides a guide for performing this optimization and analyzing the resulting performance.

In developing the theory and performing the experiments I have had a great deal of help from others. I am deeply indebted to my faculty advisor, Major Steven K. Rogers, for his continous positive support both academically and by allowing some of his best Masters students to work with me. These students, Capt Jeffery Wilson, Capt Kenneth Keppler, and Capt Thomas Burns, provided invaluable support by assembling experiments and critiquing my sometimes not too clear explanations on how things work. A special word of thanks is owed to the management and my fellow workers in the Avionics Laboratory, since without their help and support, this work would have never been completed. Finally, I wish to thank my wife Donna and three sons, Chris, Jim, and Andy, for their understanding for all of those lost hours we could have had together.

<div align="right">George A. Vogel</div>

Table of Contents

iv

List of Figures

Abstract

The introduction of two-beam coupling in photorefractive materials has resulted in an extensive amount of research into applications ranging from optical processing/computing to image amplification. This dissertation develops the theoretical equations for two-beam coupling in $BaTiO_3$. These equations, combined with the analysis of crystal performance, are applied to develop a specification which optimizes $BaTiO_3$ as an optical amplifier.

Theory predicts that, under the proper conditions, optical gains of 10^{13} are possible for nominally sized crystals of $BaTiO_3$. In practice, however, these gains are never realized due to the loss of gain to the amplification of parasitic light (beam fanning). The primary source of this parasitic light has been found to be the scattering of the pump beam from imperfections on both the crystal face and within the crystal. Through the analysis of signal and noise amplification as functions of pump and signal beam angles relative to the crystal c-axis, an optimum pump angle is defined which maximizes signal gain and minimizes the energy lost to beam fanning. The determination of an optimum gain is based upon a desired dynamic range and the crystal scattering characteristics.

A potential application for the $BaTiO_3$ optical amplifier is investigated by placing it into a confocal Fabry-Perot interferometer feedback system. With the control of mirror spacing to create destructive interferrence between the feedback and input signal the system becomes an amplifier with negative feedback. Applications for such a system include image restoration, linear amplification, and image filtering.

CHARACTERIZATION OF BARIUM TITANATE
AS AN OPTICAL AMPLIFER

I. Introduction

1.1 Background

Advances in the field of optical processing will be accelerated by the development of a high gain coherent amplifier for images of large space-bandwidth product and wide dynamic range. For good quality image amplification, the gain must be constant within a tolerable range with respect to the spatial frequency content and dynamic range of the image [8]. The primary use of an optical amplifier would be to optically interconnect stages in an optical processing scheme. Since each stage tends to introduce losses through absorption and diffraction, it is necessary to make up for these losses before going to the next stage. Another feature which would be desirable, although not necessary for many applications, is that the optical amplifier's output be coherent with respect to its input. With this feature it would be possible to use the optical amplifier with coherent feedback in a manner similar to the electrical operational amplifier (op amp).

The concept of the optical op amp was first introduced by the Soviets [17]. The development of a practical optical op amp could have the same impact upon optical processing as the electrical op amp had upon analog computing. Examples of simple applications for an optical op amp with negative feedback include; a linear image amplifier, an image integrator, an inverse optical transform, and an n by n array of parallel light amplifiers. Two or more of these applications could be connected together in a building block fashion to create even more complex applications. Furthermore, these connections could be made directly, without going

through electrical amplifiers, eliminating the bottle neck for most current optical processing approaches. In the Soviet work a number of conceptual designs are introduced which incorporate the PROM (Pockels readout optical modulator) as an op amp [21]. With the PROM a small light intensity can be used to control a large light intensity, resulting in a light amplifier. The various designs are limited, however, in that only positive feedback can be implemented. This occurs since the feedback is light intensity and intensity is always positive.

The laser amplifier might appear to be a good candidate for an optical amplifier. Some laser gain media have very high gains and are capable of producing relatively high powers with little input power. Their problem is the inability to create a useful negative feedback. Any attempt to feed back a portion of the amplifier output results in positive feedback at one or more optical frequencies. This is how the laser resonator works and is equivalent to an electric oscillator. The problem of creating a stable laser amplifier with negative feedback is tied to the speed of the amplification process and its optical bandwidth. In order to subtract light, the light beams must be coherent and 180 degrees out of phase. The gain process is so fast that the feedback signal cannot cancel/suppress the input signal before the output saturates. In other words, the optical wave is amplified in the time of the first pass through the amplifier but the feedback wave will take at least the time of one round trip, too late to affect the input.

Another optical process which might be exploited as an optical amplifier is two-beam coupling in photorefractive crystals. There has already been an extensive amount of work in this area due to the need for a light amplifier in optical processing and computing applications [33]. Two-beam coupling occurs when two coherent waves enter an electro-optic crystal and interfere with each other. Under illumination, charges are freed from the crystal lattice based upon intensity and redistributed through diffusion. The redistribution of charges causes an electro-static field to form, which in turn, modulates the index of refraction of the crystal through

the linear electro-optic (Pockel's) effect. The two interfering beams thus form a real time volume hologram in the crystal. Depending upon the particular crystal, energy from one of the beams can be diffracted into the direction of the other and, in effect, amplify the second beam.

One material which has received the most attention and appears to be very promising for two-beam coupling is $BaTiO_3$. This material has been shown to have gains in excess of 4,000 [8] and is very sensitive at reasonable light intensities. The holographic grating process is very slow to build up to the high gain condition thus giving the crystal an effective bandwidth of only a few Hertz. With this extremely narrow bandwidth it should be possible to provide a stable negative feedback by keeping the feedback optical wave 180° out of phase with respect to the input and producing destructive interference. The narrow bandwidth is required so that the gain region can be kept between the longitudinal modes of the mirror feedback system. Research has already been performed using positive coherent optical feedback and two-wave mixing in $BaTiO_3$ to perform matrix inversions [22]. Research is still ongoing to fully explain the physical processes which occur in $BaTiO_3$ so that its characteristics can be further improved [6, 16, 25].

1.2 Problem Statement

There is a requirement for a coherent optical amplifier in most optical processing designs. The amplifier must have high gain and low noise to give good dynamic range performance. Amplification time must be fast enough to compete with alternative electrical processing techniques and have good resolution to take advantage of the high information density capabilities at optical wavelengths. The process which appears most promising to create the light amplifier effect is two-wave mixing in photorefractive materials. The most promising photorefractive material is currently $BaTiO_3$. This dissertation will analyze in detail the capabilities and limitations of two-wave mixing in $BaTiO_3$ as an optical amplifier. Theory will be combined with

experimental data to characterize crystal gain, dynamic range, speed, and stability. A potential application for the BaTiO$_3$ optical amplifier will be investigated using coherent optical feedback to create a linear optical amplifier.

1.3 Sequence of Presentation

The theory of two-wave mixing in photorefractive materials will first be presented in Chapter II, with the purpose of developing a complete set of equations that can be used to describe BaTiO$_3$. These equations will then be simplified and used in Chapter III to characterize, through measurements, a typical BaTiO$_3$ crystal. The emphasis here will be on measuring basic optical amplifier characteristics including gain, dynamic range, resolution, speed, and stability. Experiments for each characteristic will be described and the resulting data presented. Finally in Chapter IV, the BaTiO$_3$ optical amplifier will be placed inside a confocal Fabry Perot resonator configuration to investigate its usefulness with coherent optical feedback. Chapter V will contain the conclusions and recommendations of this dissertation, summarize the important results and propose a crystal design which will result in an optimized optical amplifier.

II. Theory

2.1 Introduction

This chapter develops the theory and equations that will be used throughout this dissertation. First the wave equations will be defined to describe the input and output waves in terms of their optical field intensities as they propagate through the crystal. Current knowledge of photorefractive crystals will be presented with the equations which show how the input optical beams create index gratings within the crystal. Both sets of equations will then be combined to produce the photorefractive beam coupling equations which will show how the index grating affects the two optical waves. These equations will be unique from those found in the literature in that the directional relationships between all of the parameters are maintained and there are no geometry assumptions buried n the derivation. The characteristics of $BaTiO_3$ will then be used in the photorefractive beam coupling equations to develop a set of equations which are specific to $BaTiO_3$.

2.2 Wave Equations

Referring to Figure 2.1, consider the intersection of two polarized beams of coherent light inside a photorefractive crystal. The electric field of the pump $(\mathbf{E}_p)$ and signal $(\mathbf{E}_s)$ beams can be written as,

$$\mathbf{E}_p = E_p \mathbf{e}_p e^{-i(\mathbf{k}_p \cdot \mathbf{r} - \omega_p t)} + c.c. \tag{2.1}$$

$$\mathbf{E}_s = E_s \mathbf{e}_s e^{-i(\mathbf{k}_s \cdot \mathbf{r} - \omega_s t)} + c.c. \tag{2.2}$$

where E_p and E_s are the optical electric field amplitudes, $\mathbf{e}_p$ and $\mathbf{e}_s$ are the polarization unit vectors, $\mathbf{k}_p$ and $\mathbf{k}_s$ are the wave vectors of the beams, and $c.c.$ represents the complex conjugate.

The optical equations which explain how these waves are affected by the crystal can be simplified using a development similar to Yarev and Yeh [31] in their
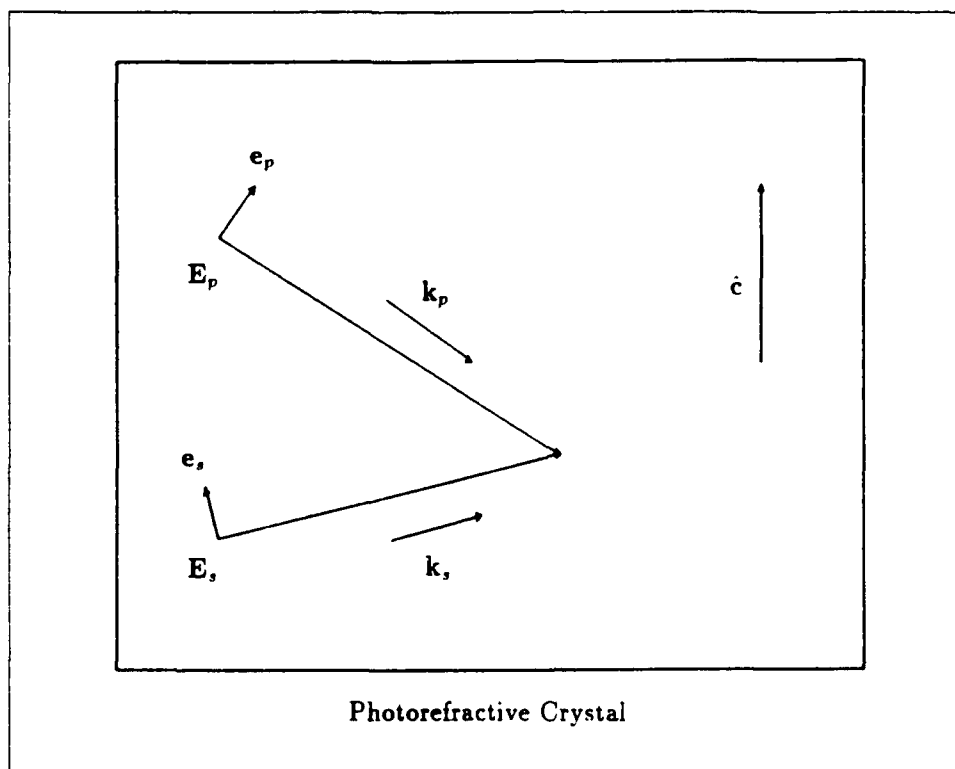
Figure 2.1. Optical Beam and Crystal Geometry

coupled-mode analysis of wave propagation in anisotropic media. The propagation of electromagnetic radiation in anisotropic media can be described in terms of normal modes of propagation. These normal modes have well-defined polarization states and phase velocities, and are obtained by diagonalizing the transverse impermeability tensor. Any wave propagation in an anisotropic medium can be decomposed into a linear combination of these normal modes with constant amplitudes. The normal modes of propagation in uniaxial crystals, such as $BaTiO_3$, consist of an ordinary wave and an extraordinary wave. The electric field vector E_o (and the displacement vector $D_o = \bar{\bar{\epsilon}}E_o$) for the ordinary wave is always perpendicular to both the c-axis and the propagation vector k_o, where $\bar{\bar{\epsilon}}$ is the dielectric permittivity tensor. The phase velocity for the ordinary wave is always the speed of light divided by the ordinary index of refraction (c/n_o), regardless of the direction of propagation. The displacement vector D_e of the extraordinary wave, is perpendicular to the propa-

gation vector, as is the electric field vector $\mathbf{E}_o$ of the ordinary wave. The electric field vector $\mathbf{E}_e$ of the extraordinary wave, however, is in general not perpendicular to the propagation vector. It lies in the plane formed by the propagation vector and the displacement vector. The electric field vectors of these two waves are mutually orthogonal. The general equation for the optical waves in the medium can be written as,

$$\mathbf{E}_{opt} = \mathbf{E}_p + \mathbf{E}_s = E_p \mathbf{e}_p e^{-i(\mathbf{k}_p \cdot \mathbf{r} - \omega_p t)} + E_s \mathbf{e}_s e^{-i(\mathbf{k}_s \cdot \mathbf{r} - \omega_s t)} + c.c. \qquad (2.3)$$

where the pump and signal polarizations are taken to be both ordinary or extraordinary. If a more general condition is required, the polarizations can be decomposed into their ordinary and extraordinary components (the normal modes) and treated in the same manner as below.

In the event that there is an external (or internal) perturbation such as stress, magnetic field, electric field, or even the presence of optical activity, the dielectric permittivity tensor in the presence of the perturbation can be written

$$\bar{\bar{\epsilon}}' = \bar{\bar{\epsilon}}_\omega + \triangle \bar{\bar{\epsilon}} \qquad (2.4)$$

where $\bar{\bar{\epsilon}}_\omega$ is the unperturbed part and $\triangle \bar{\bar{\epsilon}}$ is the change in the dielectric permittivity tensor due to the perturbation.

For this development it is advantageous to describe the wave propagation in terms of a linear combination of the unperturbed normal modes, especially when the perturbation is small (i.e., $\triangle \bar{\bar{\epsilon}} \ll \bar{\bar{\epsilon}}_\omega$). The mode amplitudes E_p and E_s are no longer constants, because $\mathbf{e}_p e^{-i(\mathbf{k}_p \cdot \mathbf{r} - \omega_p t)}$ and $\mathbf{e}_s e^{-i(\mathbf{k}_s \cdot \mathbf{r} - \omega_s t)}$ are in general, not the normal modes in the presence of the perturbation $\triangle \bar{\bar{\epsilon}}$. The total field can thus be expressed as

$$\mathbf{E}_{opt}(\mathbf{r}, t) = E_p(\mathbf{r}) \mathbf{e}_p e^{-i(\mathbf{k}_p \cdot \mathbf{r} - \omega_p t)} + E_s(\mathbf{r}) \mathbf{e}_s e^{-i(\mathbf{k}_s \cdot \mathbf{r} - \omega_s t)} + c.c. \qquad (2.5)$$

Since $\mathbf{e}_p$, $\mathbf{e}_s$, $\mathbf{k}_p$, and $\mathbf{k}_s$ are known from the solution of the unperturbed case (i.e., $\triangle \bar{\bar{\epsilon}} = 0$), the field $\mathbf{E}_{opt}$ is uniquely specified if $E_p(\mathbf{r})$ and $E_s(\mathbf{r})$ are given. The r

dependence of E_p and E_s is due to the presence of the dielectric perturbation $\triangle\bar{\bar{\epsilon}}$. The differential equations for the mode amplitudes can now be derived.

The equation governing the propagation of the optical waves through the crystal is given by the wave equation

$$\nabla^2\mathbf{E}_{opt} - \omega^2\mu(\bar{\bar{\epsilon}}_\omega + \triangle\bar{\bar{\epsilon}})\mathbf{E}_{opt} = 0 \tag{2.6}$$

It is assumed here that the medium is homogeneous and the field vectors are plane waves. The more general condition of nonplanar waves can be solved from these equations by treating the more complex waves as the sum of a set of planar waves. This approximation is valid as long as the waves have low amplitudes and create only small perturbations to the system. The longitudinal components of the electric field have been ignored by assuming that $\mathbf{k}_p \cdot \mathbf{e}_p \approx \mathbf{k}_s \cdot \mathbf{e}_s \approx 0$.

Substituting Equation 2.3 for $\mathbf{E}_{opt}$ in Equation 2.6 and assuming $\mathbf{e}_p e^{-i(\mathbf{k}_p \cdot \mathbf{r} - \omega_p t)}$ and $\mathbf{e}_s e^{-i(\mathbf{k}_s \cdot \mathbf{r} - \omega_s t)}$ are eigenmodes of the unperturbed medium,

$$[-2ik_p\frac{\partial E_p}{\partial\zeta_p} + \omega^2\mu\triangle\bar{\bar{\epsilon}}E_p]\mathbf{e}_p e^{-i(k_p\zeta_p - \omega_p t)}$$
$$+[-2ik_s\frac{\partial E_s}{\partial\zeta_s} + \omega^2\mu\triangle\bar{\bar{\epsilon}}E_s]\mathbf{e}_s e^{-i(k_s\zeta_s - \omega_s t)} = 0 \tag{2.7}$$

where $(k_p{}^2 - \omega_p{}^2\mu\bar{\bar{\epsilon}}_\omega)E_p = (k_s{}^2 - \omega_s{}^2\mu\bar{\bar{\epsilon}}_\omega)E_s = 0$. Since the waves are propagating in the $\mathbf{k}_p$ and $\mathbf{k}_s$ directions, the differential operator $\nabla\cdot$ has been replaced by $\mathbf{k}_p\frac{\partial}{\partial\zeta_p}$ and $\mathbf{k}_s\frac{\partial}{\partial\zeta_s}$ respectively, where ζ is the distance along the direction of propagation (i.e., $\zeta_p = \hat{\mathbf{k}}_p \cdot \mathbf{r}$ and $\zeta_s = \hat{\mathbf{k}}_p \cdot \mathbf{r}$). It has also been assumed that E_p and E_s are slowly varying functions of $\mathbf{r}$, so that $(\frac{\partial^2 E_p}{\partial\zeta_p{}^2}) \ll k_p\frac{\partial E_p}{\partial\zeta_p}$ and $(\frac{\partial^2 E_s}{\partial\zeta_s{}^2}) \ll k_s\frac{\partial E_s}{\partial\zeta_s}$.

Equation 2.7 shows how the amplitudes of the pump and signal optical waves are affected by the perturbation in the dielectric permittivity tensor. If $\triangle\bar{\bar{\epsilon}}$ was equal to zero, then the two waves would be independent and they would propagate through the medium with their amplitudes unchanged. The next section will derive an expression for $\triangle\bar{\bar{\epsilon}}$ and show how it couples the pump and signal beams so that one beam will increase in amplitude at the expense of the other.

2-4

2.3 Photorefractive Theory

The photorefractive effect is a phenomenon in which the local index of refraction is changed by a spatial variation of the light intensity. Such an effect was first reported in 1966 [2]. The spatial index variation leads to distortion of the wavefront and has been since observed in many electro-optic crystals including $LiNbO_3$, $BaTiO_3$, SBN, BSO, BGO, GaAs, InP, etc. The process has been described by numerous authors [10, 12, 18, 19, 29] and can be summarized as follows. It is generally believed that the photorefractive effect arises from optically generated charge carriers that migrate when the crystal is exposed to a spatially varying pattern of illumination with photons having sufficient energy. Migration of charge carriers due to drift or diffusion produces a space-charge separation, which then gives rise to a space-charge field. Such a field induces a refractive index change via the Pockels effect. This process is shown in Figure 2.2. Notice from this simple diagram that the phase of the index grating is in general out of phase with respect to the intensity grating. This phase shift will eventually determine how the two optical waves are coupled.

Although there are several models for the photorefractive effect, [10, 12, 18, 19, 29] the Kukhtarev - Vinetskit solid state model is the most widely accepted one. In this model photorefractive materials are assumed to contain donor and acceptor traps that arise from imperfections in the crystal. These traps create intermediate electronic energy states in the bandgap of the insulators. When photons with sufficient energy are present, electronic transitions due to photoexcitation take place. As a result of the transitions, charge carriers are excited into the conduction band and the ionized donors become empty trap sites. The response of the photorefractive medium to the incident light may be described by the charge transport equations of Kukhtarev et al [18].

(a) Intensity

(b) Photo-Induced Space-Charge Density

(c) Space-Charge Electric Field

(d) Photo-Induced Refractive Index Grating
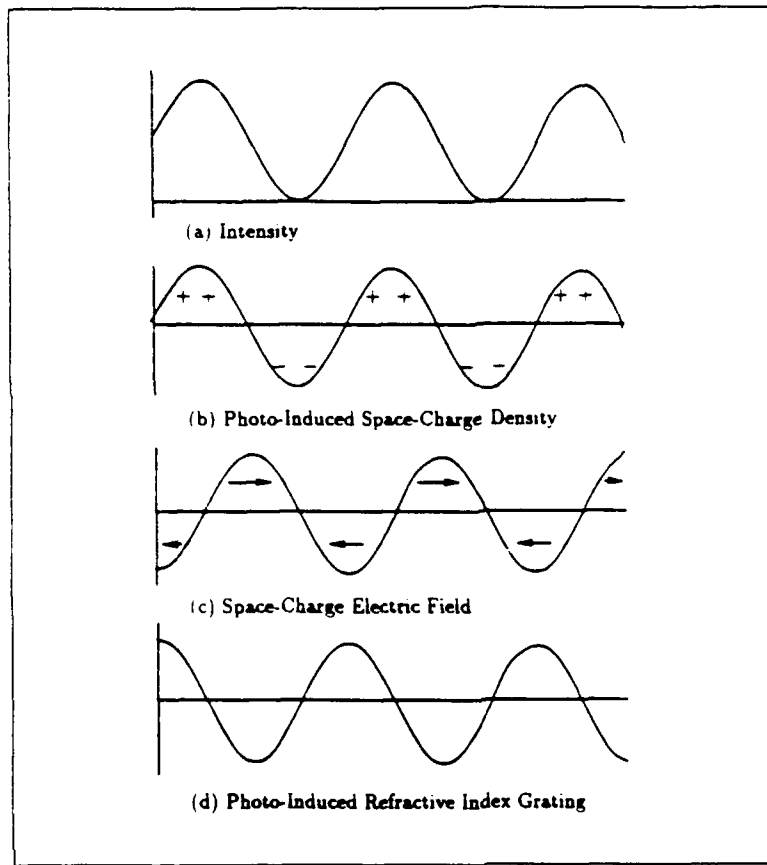
Figure 2.2. Charge and Index Distribution in the Crystal

$$\frac{\partial N_D^+}{\partial t} = (sI + \beta_T)(N_D - N_D^+) - \gamma_R N N_D^+ \tag{2.8}$$

$$\mathbf{j} = e\mu N\mathbf{E} - k_B T \mu \nabla N + pI\hat{c} \tag{2.9}$$

$$\nabla \cdot \mathbf{j} = e(\frac{\partial}{\partial t} N_D^+ - \frac{\partial}{\partial t} N) \tag{2.10}$$

$$\nabla \cdot (\epsilon_s \mathbf{E}) = 4\pi e(N_A + N - N_D^+) \tag{2.11}$$

Equation 2.8 represents the effective rate in which the donors are ionized and is a function of the carrier generation and recombination rates. The rate of carrier

generation is $(sI + \beta_T)(N_D - N_D{}^+)$ in which s is the cross section of photoionization, I is the light intensity, β_T is the rate of thermal generation, N_D is the concentration of donors and $N_D{}^+$ is the concentration of ionized traps. The rate of recombination, or trap capture, is $\gamma_R N N_D{}^+$ in which γ_R is the carrier-ionized trap recombination rate and N is the concentration of the carriers.

Equation 2.9 represents the crystal current density (**j**) resulting from drift, diffusion, and photovoltaic effects. The drift current is $e\mu N\mathbf{E}$ in which e is the electronic charge, μ is the mobility and $\mathbf{E} = \mathbf{E}_0 + \mathbf{E}_{sc}$ is the sum of the applied and space charge fields respectively. The diffusion current is given by $-k_B T \mu \nabla N$ in which k_B is Boltzmann's constant and T is the absolute temperature. The photovoltaic current is $pI\hat{c}$ in which p is the photovoltaic constant and $\hat{c}$ is a unit vector along the c-axis of the crystal.

Equation 2.10 and Equation 2.11 represent the Continuity and Poisson's equations respectively. Equation 2.10 simply states that the difference between the rate in which carriers enter a region and the rate in which they leave it is equal to the rate of charge creation/destruction inside the region. Equation 2.11 is used to describe how the space charge electric field is created based upon the total charge density distribution. In this equation ϵ_s is the static dielectric constant and N_A is the number density of negatively charged ions that compensate for the charge of $N_D{}^+$ in the dark.

Following the development by Valley [27], the solution for Equations 2.7 - 2.11 is most easily performed by solving Equations 2.8 - 2.11 for E_{sc} using the optical field given by Equation 2.5. An expression for the perturbation in the dielectric permittivity tensor in terms of the space charge field is then found so that Equation 2.7 can be solved.

First eliminate N_D^+ and N from Equations 2.8 and 2.11 to obtain,

$$\nabla \cdot \frac{\partial}{\partial t}(\epsilon_s \mathbf{E}) = -4\pi \nabla \cdot \mathbf{j} \tag{2.12}$$

This was accomplished by differentiating Equation 2.11 with respect of time and assuming that N_A is effectively constant. Equation 2.12 may be integrated to give,

$$\epsilon_s \frac{\partial \mathbf{E}}{\partial t} = -4\pi \mathbf{j} + 4\pi \mathbf{J} \tag{2.13}$$

where $4\pi \mathbf{J}$ is the integration constant. $\mid \mathbf{J} \mid A_{ELECTRODE}$ is the current in the external circuit that would be used to apply the external field E_0 to the crystal over the electrode area $A_{ELECTRODE}$. Next, both N_D^+ and $\mathbf{j}$ may be eliminated from Equations 2.8 - 2.11 and 2.13 to obtain [20],

$$\epsilon_s \frac{\partial \mathbf{E}}{\partial t} = -4\pi(e\mu N\mathbf{E} - k_B T\mu\nabla N + pI\hat{c}) + 4\pi \mathbf{J} \tag{2.14}$$

$$\frac{\partial N}{\partial t} = (\beta_T + sI)N_D + (\beta_T + sI + \gamma_R N)(\frac{\epsilon_s}{4\pi e}\nabla \cdot \mathbf{E} - N - N_A)$$
$$- \frac{1}{e}\nabla \cdot (e\mu N\mathbf{E} - k_B T\mu\nabla N + pI\hat{c}) \tag{2.15}$$

The optical waves generate an interference pattern inside the crystal proportional to,

$$\mathbf{E}_{opt}\mathbf{E}_{opt}^* = E_p^2 + E_s^2 + \{E_p E_s(\mathbf{e}_p \cdot \mathbf{e}_s)exp[-i(\mathbf{k}_g \cdot \mathbf{r} - \Delta\omega t)] + c.c.\} \tag{2.16}$$

where $\mathbf{k}_g = \mathbf{k}_s - \mathbf{k}_p$ is the grating wave vector and $\Delta\omega = \omega_s - \omega_p$ is the difference in the signal and pump optical frequencies.

Since the rate of carrier generation and the resulting number of carriers is dependent upon the light intensity as shown in Equation 2.15 and the intensity is proportional to $\mathbf{E}_{opt}\mathbf{E}_{opt}^*$, it is reasonable to assume that Equations 2.14 and 2.15 can be solved by letting N and $\mathbf{E}$ take the form,

$$N = N_0 + N_1(\mathbf{r})exp[i(\mathbf{k}_g \cdot \mathbf{r} - k_g vt)] + N_{-1}(\mathbf{r})exp[-i(\mathbf{k}_g \cdot \mathbf{r} - k_g vt)] \tag{2.17}$$

$$\mathbf{E} = \mathbf{E}_0 + \mathbf{E}_1(\mathbf{r})exp[i(\mathbf{k}_g \cdot \mathbf{r} - k_g vt)] + \mathbf{E}_{-1}(\mathbf{r})exp[-i(\mathbf{k}_g \cdot \mathbf{r} - k_g vt)] \tag{2.18}$$

where $v = \Delta\omega/k_g$ is the velocity of the moving grating in the crystal resulting from ω_p and ω_s being slightly different optical frequencies. Equations 2.17 and 2.18 assume

that the alternating components are small perturbations and that the higher-order Bragg components can be neglected. The a.c. component of the electric field shown in Equation 2.18 is the space charge field that will result from the redistribution of charges.

Substitution of Equations 2.5, 2.17 and 2.18 into Equations 2.14 and 2.15 yields,

$$- i k_g v \epsilon_s \mathbf{E}_1 = -4\pi(e\mu N_0 \mathbf{E}_1 + e\mu N_1 \mathbf{E}_0 - i k_B T \mu N_1 \mathbf{k}_g + pa E_p E_s (\mathbf{e}_p \cdot \mathbf{e}_s)\hat{\mathbf{c}}) \quad (2.19)$$

$$-i k_g v N_1 =$$

$$s N_D a E_p E_s (\mathbf{e}_p \cdot \mathbf{e}_s) + (\beta + s I_0 + \gamma_R N_0)(\frac{i\epsilon_s}{4\pi e} k_g E_1 - N_1)$$

$$- i \frac{k_g}{e} [e\mu E_0 E_1 + e\mu N_1 (\mathbf{E}_0 \cdot \hat{\mathbf{k}}_g) - i k_B T \mu k_g N_1 + pa E_p E_s (\mathbf{e}_p \cdot \mathbf{e}_s)(\hat{\mathbf{k}}_g \cdot \hat{\mathbf{c}})]$$

$$+ (s a E_p E_s (\mathbf{e}_p \cdot \mathbf{e}_s) + \gamma_R N_1)(-N_0 - N_A) \quad (2.20)$$

$$(\beta_T + s I_0)(N_D - N_A - N_0) + \gamma_R(N_A + N_0)N_0 = 0, \quad (2.21)$$

where I_0 is the average optical intensity and $\hat{\mathbf{k}}_g$ is a unit vector in the $\mathbf{k}_g$ direction. Equation 2.21 was obtained by retaining the real, first-order components from Equation 2.15. For irradiances typical of cw laboratory experiments ($N_0 \ll N_A$ and $N_0 \ll N_D - N_A$),

$$N_0 \approx (\beta_T + s I_0)(N_D - N_A)/\gamma_R N_A \quad (2.22)$$

Also, the parameter a relates the optical field to the intensity:

$$a = c n_b/4\pi \quad (2.23)$$

$$I_0 = a(| E_p |^2 + | E_s |^2) \quad (2.24)$$

where c is the speed of light and n_b is the background refractive index.

Elimination of N_1 in favor of E_1 yields

$$\{[-ik_g v + (\frac{1}{\tau_1}) + (\frac{1}{\tau_R}) + (\frac{i}{\tau_E})(\hat{E}_0 \cdot \hat{k}_g) + (\frac{1}{\tau_D})][-ik_g v + (\frac{1}{\tau_{di}})]\hat{E}_1$$

$$-[(\frac{i}{\tau_2}) - (\frac{i}{\tau_{di}})][(\frac{-\hat{E}_0}{\tau_E}) + (\frac{i\hat{k}_g}{\tau_D})]\}E_1 =$$

$$-(\mathbf{E}_0 - iE_D\hat{k}_g)\frac{1}{\tau_{di}\tau_R}\frac{E_p E_s(\mathbf{e}_p \cdot \mathbf{e}_s)}{|E_p|^2 + |E_s|^2} \qquad (2.25)$$

where:

$\tau_{di} = \epsilon_s/(4\pi e\mu N_0)$, dielectric relaxation time;

$\tau_E = 1/(k_g\mu E_0)$, drift time;

$\tau_D = e/(\mu k_B T k_g^2)$, diffusion time;

$\tau_R = 1/(\gamma_R N_A)$, electron recombination time;

$\tau_1 = 1/(\beta_T + sI_0 + 2\gamma_R N_0)$, inverse sum of thermal production, photo production and twice ion recombination rates;

$\tau_2 = 1/(\beta_T + sI_0 + \gamma_R N_0)$, inverse sum of thermal production, photo production and ion recombination rates;

$E_D = k_B T k_g/e$, field set up due to carrier diffusion.

Equation 2.25 reflects the assumption that conditions for Equation 2.22 hold and that the photovoltaic contribution can be ignored. $\hat{E}_0$ and $\hat{E}_1$ are unit vectors in the $\mathbf{E}_0$ and $\mathbf{E}_1$ directions respectively. This equation is unique in that it retains the vectorial relataionships between the grating and the external electric field. From this equation it can be shown that in the absence of an external electric field, or when this field is applied in a direction parallel to the grating vector, the space charge field will be in the direction of the grating vector. If $\mathbf{E}_0$ is not parallel to $\mathbf{k}_g$ then 2.26 would have to be solved by resolving the equation into components parallel and perpendicular to the grating vector and solving for E_1 and its vector direction, $\hat{E}_1$, simultaneously. To keep these equations as simple as possible, $\mathbf{E}_0$ will be required to be parallel to the grating vector $\mathbf{k}_g$. With this simplification, the vectorial portions

of Equation 2.25 can be made scalar for the following derivation and will give results which agree with Valley [27].

For typical irradiances, $1/\tau_1$ is much smaller than $1/\tau_R$ and typical frequency shifts $k_g v$ are of the order of a few hertz, whereas τ_E is typically less than 10μsec so that $k_g v \ll \tau_E^{-1}$. Using these approximations in Equation 2.25 yields,

$$(A + Bu)E_1 = -(E_0 - iE_D)E_p E_s(\mathbf{e}_p \cdot \mathbf{e}_s)/(|\ E_p\ |^2 + |\ E_s\ |^2) \tag{2.26}$$

$$E_{-1} = E_1^* \tag{2.27}$$

where:

$$A = 1 + \frac{E_D}{E_q} + \frac{iE_0}{E_q},$$

$$B = \frac{E_0}{E_q} - \frac{i\tau_{di}}{\tau_2} - \frac{iE_D}{E_q},$$

$$u = k_g v \tau_2,$$

$$E_q = \frac{eN_A}{\epsilon_0\epsilon_s k_g}\left(1 - \frac{N_A}{N_D}\right)$$

Solving Equation 2.26 for E_1 and rationalizing the denominator results in,

$$E_1 = g(u)E_q\frac{E_p E_s(\mathbf{e}_p \cdot \mathbf{e}_s)}{I_0} \tag{2.28}$$

where,

$$g(u) = \frac{-\{\frac{E_0}{E_q} + (\frac{E_0^2}{E_q^2} + \frac{E_D^2}{E_q^2} + \frac{E_D}{E_q}\frac{\tau_{di}}{\tau_2})u\} + i\{\frac{E_D}{E_q} + \frac{E_D^2}{E_q^2} + \frac{E_0^2}{E_q^2} + \frac{E_0}{E_q}\frac{\tau_{di}}{\tau_2}u\}}{[1 + \frac{E_D}{E_q} + \frac{E_0}{E_q}u]^2 + [\frac{E_0}{E_q} - \frac{\tau_{di}}{\tau_2}u - \frac{E_D}{E_q}u]^2} \tag{2.29}$$

This equation is unique to this dissertation in that it breaks out and defines $g(u)$ as a unitless expression containing most of the photorefractive crystal material characteristics, the external electric field, and the factor u which varies with the difference between the pump and signal optical frequencies.

Equation 2.28 has been derived showing how the space charge field is related to the pump and signal beams and their characteristics as well as the photorefractive material and its characteristics. It is this space charge field which will create the refractive index grating through the Pockels effect and produce the resulting photorefractive beam coupling equations discussed in the next section.

2.4 Photorefractive Beam Coupling

As the pump and signal beams pass through the crystal, their electric field intensities will be coupled through an index grating their mutual interference created. This relationship has been derived and expressed in Equation 2.7 in terms of a perturbation in the dielectric permittivity tensor. The relationship between $\triangle \bar{\bar{\epsilon}}$ and the space charge field $\mathbf{E}_{sc}$ is found by calculating the perturbation to the impermeability tensor as $\triangle \bar{\bar{b}} = R \cdot \mathbf{E}_{sc}$ where R is the linear electro-optic tensor. The dielectric permittivity tensor is found by taking the inverse of the impermeability tensor using a first order series expansion. The perturbation to the dielectric permittivity tensor is thus [10]

$$\triangle \bar{\bar{\epsilon}} = -\bar{\bar{\epsilon}}_\omega \cdot R \cdot \mathbf{E}_{sc} \cdot \bar{\bar{\epsilon}}_\omega \tag{2.30}$$

where the space charge field was found in the previous section as

$$\mathbf{E}_{sc} = E_1 \hat{\mathbf{k}}_g e^{-i(\hat{\mathbf{k}}_g \cdot \mathbf{r} - k_g vt)} + E_{-1} \hat{\mathbf{k}}_g e^{i(\hat{\mathbf{k}}_g \cdot \mathbf{r} - k_g vt)} \tag{2.31}$$

The wave equation given by Equation 2.7 can now be used to generate the differential equations for $\mathbf{E}_p$ and $\mathbf{E}_s$ by scalar multiplying by $\mathbf{e}_p$ and $\mathbf{e}_s$ and considering only those waves propagating in the $\mathbf{k}_p$ and $\mathbf{k}_s$ directions.

$$\frac{\partial E_p}{\partial \zeta_p} = \frac{\omega^2 \mu \epsilon_0}{2 k_p} R_{eff} Im[g^*(u)] E_q E_p \frac{E_p E_s (\mathbf{e}_p \cdot \mathbf{e}_s)}{|E_p|^2 + |E_s|^2} \tag{2.32}$$

$$\frac{\partial E_s}{\partial \zeta_s} = \frac{\omega^2 \mu \epsilon_0}{2 k_s} R_{eff} Im[g(u)] E_q E_s \frac{E_p E_s (\mathbf{e}_p \cdot \mathbf{e}_s)}{|E_p|^2 + |E_s|^2} \tag{2.33}$$

where R_{eff} is the effective electro-optic coefficient and is given by

$$R_{eff} = \mathbf{e}_p \cdot \bar{\bar{\epsilon}}_\omega \cdot R \cdot \hat{\mathbf{k}}_g \cdot \bar{\bar{\epsilon}}_\omega \cdot \mathbf{e}_s = \mathbf{e}_s \cdot \bar{\bar{\epsilon}}_\omega \cdot R \cdot \hat{\mathbf{k}}_g \cdot \bar{\bar{\epsilon}}_\omega \cdot \mathbf{e}_p \tag{2.34}$$

The solution to Equations 2.32 and 2.33 has been found by Kukhtarev [18]

$$\frac{\partial I_p}{\partial \zeta_p} = -\Gamma I_p \frac{(I_0 - I_p)}{I_0} \tag{2.35}$$

$$\frac{\partial I_s}{\partial \zeta_s} = \Gamma I_s \frac{(I_0 - I_s)}{I_0} \tag{2.36}$$

where Γ is the exponential gain coefficient,

$$\Gamma = \frac{2\pi(\mathbf{e}_p \cdot \mathbf{e}_s)}{n_b \lambda_0} R_{eff} Im[g(u)] E_q \qquad (2.37)$$

where λ_0 is the vacuum wavelength of the light.

Equations 2.35 and 2.36 have solutions in the form [18],

$$I_p(\zeta_p) = \frac{I_0}{1 + m_0 e^{\Gamma \zeta_p}} \qquad (2.38)$$

$$I_s(\zeta_s) = \frac{I_0}{1 + \frac{1}{m_0} e^{-\Gamma \zeta_s}} \qquad (2.39)$$

where,

$$m_0 = \frac{I_s(0)}{I_p(0)} \qquad (2.40)$$

is the signal-to-pump ratio with $I_p(0)$ and $I_s(0)$ defined as the pump and signal intensities as the beams enter the crystal.

If the crystal absorption coefficient α is to be accounted for, the above equations become [18]

$$\frac{\partial I_p}{\partial \zeta_p} = -\Gamma I_p \frac{(I_0 - I_p)}{I_0} - \alpha I_p \qquad (2.41)$$

$$\frac{\partial I_s}{\partial \zeta_s} = \Gamma I_s \frac{(I_0 - I_s)}{I_0} - \alpha I_s \qquad (2.42)$$

$$I_p(\zeta_p) = \frac{I_0 e^{-\alpha \zeta_p}}{1 + m_0 e^{\Gamma \zeta_p}} \qquad (2.43)$$

$$I_s(\zeta_s) = \frac{I_0 e^{-\alpha \zeta_s}}{1 + \frac{1}{m_0} e^{-\Gamma \zeta_s}} \qquad (2.44)$$

All of the above equations are for two-beam coupling in steady state. During grating formation, charge densities are redistributed at a rate determined by the average charge density and the charge mobility. All of the above equations can be modified to include time by using the steady state Γ to get [24]

$$\Gamma_t(t) = \Gamma(1 - e^{-\frac{t}{\tau_{di}}}) \qquad (2.45)$$

2-13

Recall that τ_{di} is the dielectric relaxation time and is inversely proportional to the charge mobility and the average charge carrier density, which is in turn proportional to I_0. Thus the rate in which the crystal builds a grating is proportional to the total intensity of the light passing through it.

The pump and signal beam intensities, normalized by $I_p(0)$, are plotted in Figure 2.3 as functions of ζ. For this plot a typical $\Gamma = 2/mm$ and $m_0 = 10^{-4}$ have been selected. As the signal beam traverses the crystal, its intensity increases exponentially until it becomes comparable to the pump beam intensity. Beyond this point ($\zeta \approx 4mm$ in the plot) the gain process saturates and the pump beam intensity begins to decrease, a condition commonly referred to as pump depletion. Notice that if $I_s(0)$ is increased then I_s would saturate for a smaller ζ. This process is shown in Figure 2.4 by plotting crystal gain $G = I_s/I_s(0)$ as a function of input signal intensity $I_s(0)$ for a constant ζ. This plot represents a typical measurement made in a two-beam coupling experiment.

The complete set of equations have been defined for understanding the two-beam coupling process in photorefractive crystals. It should be remembered, however, that along the way a number of simplifying assumptions have been made which may not apply to some crystals. The next section further narrows these equations by applying them to $BaTiO_3$.

2.5   Beam Coupling in $BaTiO_3$

The equation for Γ given by Equation 2.37 contains all of the critical parameters required for characterizing the two-beam coupling gain in photorefractive materials and can now be used to further understand $BaTiO_3$. E_q is the saturation electric field and contains those material parameters which affect the strength of the maximum space charge electric field for a given set of conditions. The function $g(u)$ is the normalized gain coefficient as a function of the difference between the pump and signal optical frequencies and has a maximum of $E_D/(E_D + E_q)$ when $u = 0$ and
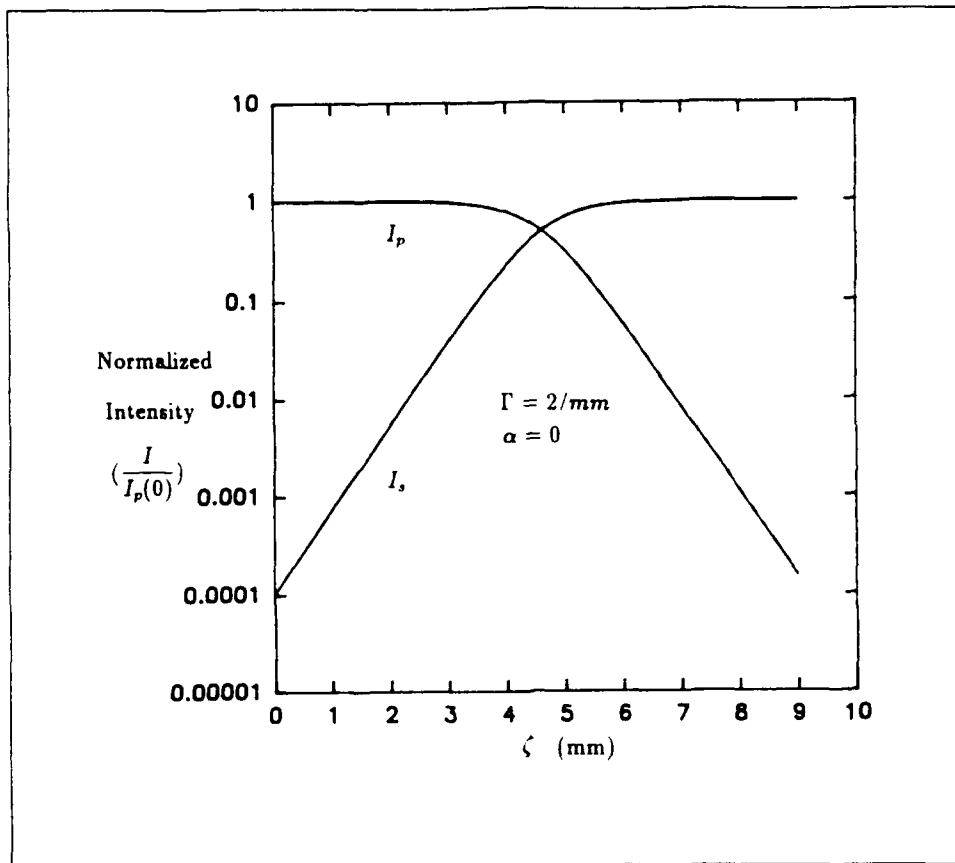
Figure 2.3. Theoretical Pump and Signal Intensities vs Path Length

$E_0 = 0$. Both E_q and $g(u)$ are functions of the crystal and beam geometries since they vary with k_g and its relationship to the c-axis. The effective electro-optic coefficient is a very strong function of these geometries and can change significantly for small changes in the pump and signal beam angles.

Figure 2.5 shows the optical geometrical configuration assumed for this research. The principle coordinate system of the crystal is chosen, thus making the z-axis parallel to the crystal c-axis. In general the c-axis is not necessarily parallel to the face of the crystal. The two beams with unit polarization vectors e_p and e_s intersect in the crystal at the angles θ_p and θ_s from the c-axis. The angle between the two beams is 2θ where $\theta = (\theta_s - \theta_p)/2$. These intersecting beams create an interference pattern with grating wavevector k_g which is also in the y-z plane. This grating

Figure 2.4. Theoretical Gain vs Normalized Input Signal Intensity

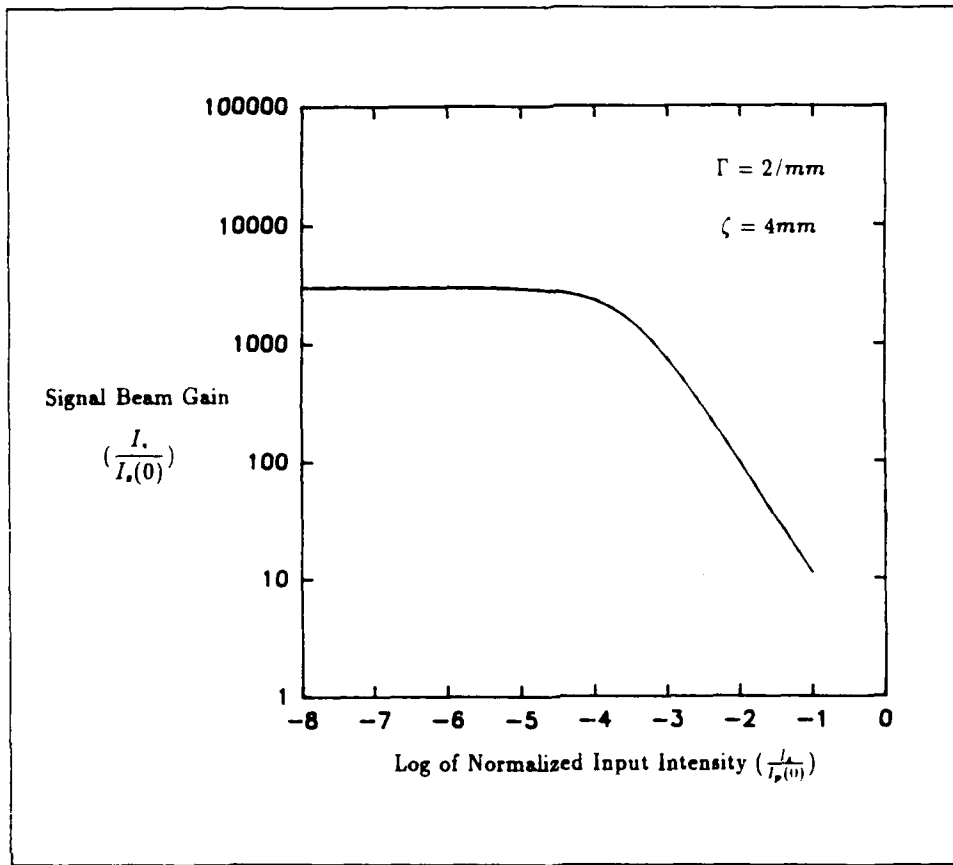wavevector creates an angle β with respect to the c-axis where $\beta = (\theta_s + \theta_p)/2 - 90°$.

The dielectric permittivity and contracted electro-optic (Pockels) coefficient tensors for BaTiO$_3$ are given by,

$$\bar{\bar{\epsilon}}_\omega = \begin{pmatrix} n_o^2 & 0 & 0 \\ 0 & n_o^2 & 0 \\ 0 & 0 & n_e^2 \end{pmatrix} \tag{2.46}$$
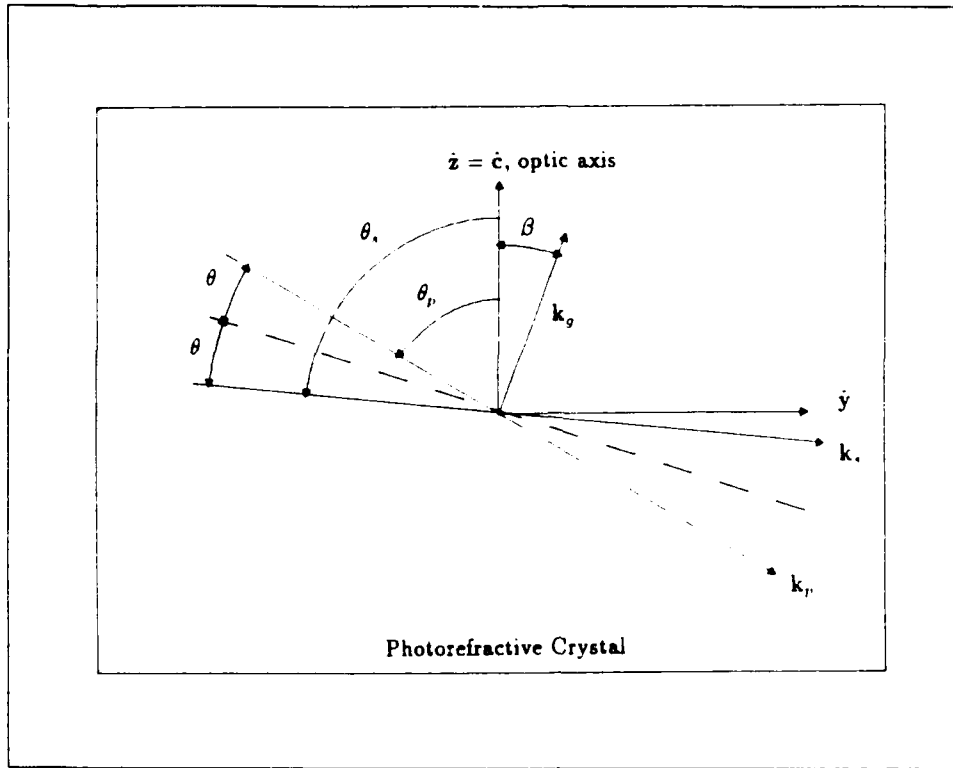
Figure 2.5. Optical Geometrical Configuration with Assigned Angles

and

$$R = \begin{pmatrix} 0 & 0 & r_{13} \\ 0 & 0 & r_{13} \\ 0 & 0 & r_{33} \\ 0 & r_{42} & 0 \\ r_{42} & 0 & 0 \\ 0 & 0 & 0 \end{pmatrix}$$

(2.47)

respectively. For $BaTiO_3$ at $\lambda = 514.5$ nm, the ordinary and extraordinary indicies are given by $n_o = 2.488$ and $n_e = 2.424$. The nonzero, linear electro-optic coefficients are $r_{13} = 8$, $r_{33} = 28$, and $r_{42} = 820$, in units of 10^{-12} m/V. The exceptionally large value of the r_{42} coefficient will yield a high value of R_{eff} when both beams are extraordinarily polarized and they interfere to generate a grating with nonzero β.

Equation 2.34 can now be solved in terms of the above geometries. Let $\hat{k}_g =$

$(0, \sin \beta, \cos \beta)$ and first solve for the quantity between the unit polarization vectors.

$$\bar{\bar{\epsilon}}_\omega \cdot R \cdot \hat{k}_g \cdot \bar{\bar{\epsilon}}_\omega = \begin{pmatrix} n_o{}^4 r_{13} \cos \beta & 0 & 0 \\ 0 & n_o{}^4 r_{13} \cos \beta & n_o{}^2 n_e{}^2 r_{42} \sin \beta \\ 0 & n_o{}^2 n_e{}^2 r_{42} \sin \beta & n_e{}^4 r_{33} \cos \beta \end{pmatrix} \qquad (2.48)$$

When performing this calculation it was necessary to convert from contracted indices to uncontracted indices as in Yariv [31, pg 222].

Three conditions are now considered in which the input beams have: ordinary polarization (perpendicular to the plane of intersection and the c-axis), extraordinary polarization (in the plane of intersection), and orthogonal polarizations (one beam ordinary polarization and one beam extraordinary polarization).

Case I: Ordinary polarization,

$$\mathbf{e}_p = \mathbf{e}_s = (1, 0, 0)$$

$$R_{eff(o)} = n_o{}^4 r_{13} \cos \beta \qquad (2.49)$$

Case II: Extraordinary polarization,

$$\mathbf{e}_p = (0, \cos \theta_p, \sin \theta_p)$$

$$\mathbf{e}_s = (0, \cos \theta_s, \sin \theta_s)$$

$$R_{eff(e)} = \frac{1}{2} \{ n_o{}^4 r_{13}(\cos 2\theta - \cos 2\beta) + 4 n_o{}^2 n_e{}^2 r_{42} \sin^2 \beta + n_e{}^4 r_{33}(\cos 2\theta + \cos 2\beta) \} \cos \beta \qquad (2.50)$$

Case III: One beam ordinary polarization and the other extraordinary polarization,

$$\mathbf{e}_p = (1, 0, 0)$$

$$\mathbf{e}_s = (0, \cos \theta_s, \sin \theta_s)$$

$$R_{eff(x)} = 0 \qquad (2.51)$$

2-18

Case III demonstrates that $BaTiO_3$ does not exhibit any cross-polarization two-beam mixing [34, 35] so that each polarization condition can be considered separately. Case I shows $R_{eff(o)}$ to be relatively small since it only accesses the small r_{13} component of the electro-optic tensor. Case II provides the most potential for getting the largest $R_{eff(e)}$ by being able to access the large r_{42} component through the selection of appropriate θ and β values. The saturation electric field E_q is also a function of beam and crystal geometry through the effective static dielectric constant ϵ_s of $BaTiO_3$. The static dielectric tensor $\bar{\epsilon}_s$ for $BaTiO_3$ is given by

$$\bar{\epsilon}_s = \begin{pmatrix} \epsilon_1 & 0 & 0 \\ 0 & \epsilon_2 & 0 \\ 0 & 0 & \epsilon_3 \end{pmatrix} \qquad (2.52)$$

in the principle coordinate system with $\epsilon_1 = \epsilon_2 = 3600$ and $\epsilon_3 = 135$ [31]. The value of ϵ_s in the direction of the grating is found by $\epsilon_s = \hat{k}_g \cdot \bar{\epsilon}_s \cdot \hat{k}_g$ and results in

$$\epsilon_s = \epsilon_1 \sin^2(\beta) + \epsilon_3 \cos^2(\beta) \qquad (2.53)$$

The exponential gain coefficient is plotted in Figure 2.6 as a function of β and for various θ's. A charge density of $2 \times 10^{16}/cm^3$ was assumed for these calculations. It is also interesting to note that the diffusion field is found to be

$$E_D = (1.5 \times 10^6 v/m) \sin \theta$$

and the saturation electric field is found to be

$$E_q = (6.1 \times 10^6 v/m)/(\epsilon_s \sin \theta)$$

for this charge density. Thus the diffusion field dominates the saturation field if $\theta > 9.8°$ - $2.6°$ for $\beta = 0°$ - $45°$ respectively. From Figure 2.6 it can be seen that Γ is optimized for $\beta \approx 45°$ and $\theta \approx 2°$ - $5°$. It is this basic relationship which led Fainman [8] to recommend the $45°$-cut $BaTiO_3$ as an optimized optical amplifier. Although he uses a slightly different set of reference angles, these equations are also consistent with Valley [28].
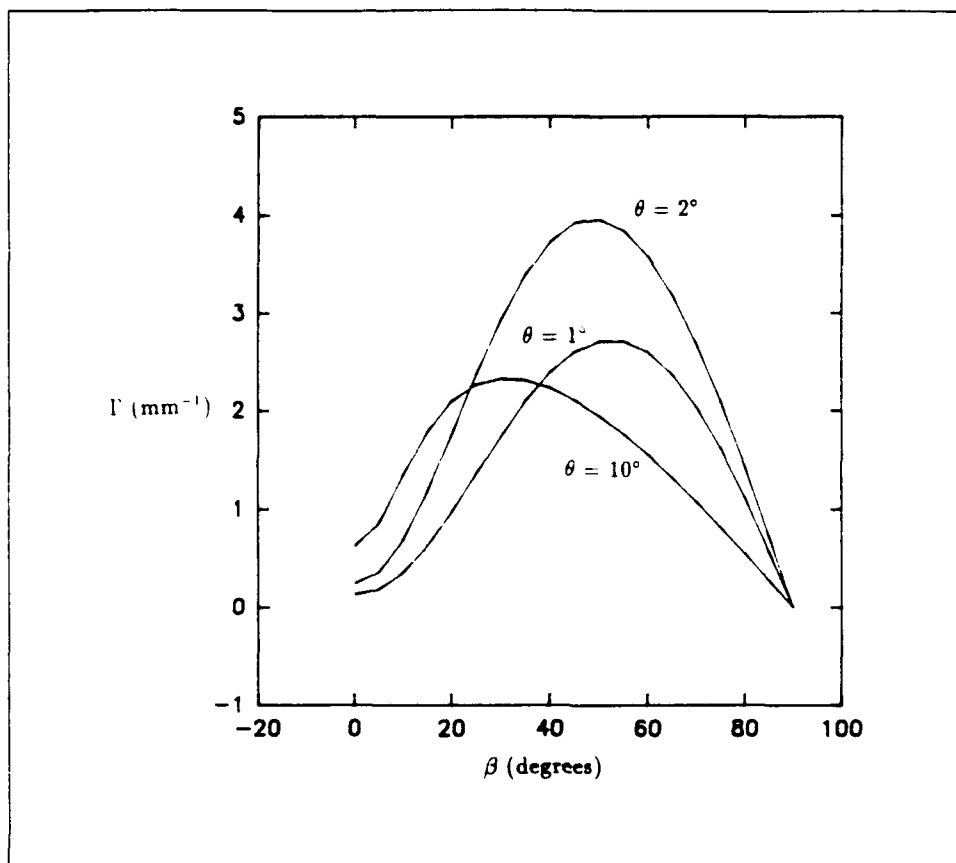
Figure 2.6. Optical Gain Coefficient in BaTiO$_3$ as a Function of β and θ.

2.6 Summary

This chapter has developed the theoretical equations for optical gain using two-beam coupling in BaTiO$_3$. These equations will be used in the next chapter to characterize BaTiO$_3$ crystals and to show how input beam angles can be used to control the amplifier gain and output signal-to-noise. These equations are as general as possible so that they can include the factors of pump and signal beam polarizations, optical frequencies, and their angles relative to the crystal c-axis. Also included, but not used in this dissertation, is the external electric field and its orientation to the crystal c-axis. All equations developed in this chapter which have explicit angles are for k_p, k_s, and the c-axis in the same plane. A simple computer program has been written around the more general vectorial equations to calculate Γ for arbitrary

input beam angles. This program will be used in the next chapter to help explain the gain realized by randomly scattered pump beam light.

III. Barium Titanate as an Image Amplifier

3.1 Light Amplifier Concerns

A simple configuration for a coherent light amplifying system is shown in Figure 3.1. The variables x and y are used here to explicitly show that the fields are images and that they vary across their respective image planes. Input information in the form of an image, $E_{in}(x,y)$, is introduced to the amplifier through input optics L_{in}. These input optics are shown here as a simple lens but could be more complex if modification to the input is desired to optimize the amplifier performance. The light amplifier, LA, is shown as a simple cube and could be placed in the image or Fourier planes of the optics. Since it is assumed the amplifier is using two-beam coupling as the gain process, a pump beam, I_p, is also shown. Practical considerations must be made to introduce the pump without interfering with the input image. The output optics, L_{out}, like the input optics, could be more complex than the simple lens shown. These optics are required to present the amplified image to a readout device or another optical processing or amplifier stage. Depending upon the gain of the light amplifier and the coherence of its output, the output image can be fed back and combined coherently with the input image to perform additional optical processing applications.

Equation 3.1 gives the relationship between $E_{in}(x,y)$ and $E_{out}(x,y)$ so that the more practical aspects of the light amplifier can be discussed. The optical gain and point spread function of the LA in conjunction with the input and output optics is represented by $G(x,y)$. The "∗" represents a two-dimensional convolution, $N_1(x,y)$ represents noise present with the input image and any other noise sources which will be amplified, and $N_2(x,y)$ represents all other additive noise sources affecting the output.

$$E_{out}(x,y) = G(x,y) * [E_{in}(x,y) + N_1(x,y)] + N_2(x,y) \qquad (3.1)$$
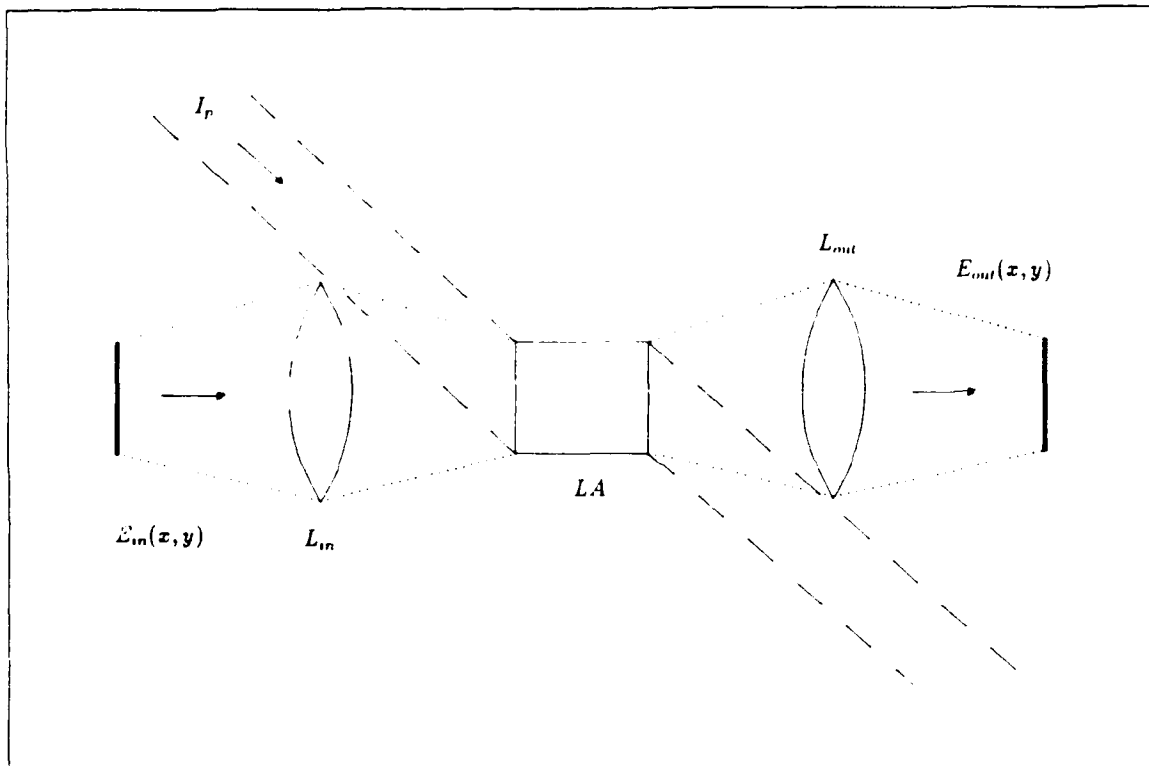
Figure 3.1. Optical Amplifier Concept

Good optical design can minimize the effects of finite input and output optics so that they do not significantly degrade the input image. Since most light amplifiers are of limited size, they are placed in the optical system where they can collect the throughput energy most efficiently. Typically this is in an image or Fourier plane. In either case, the light amplifier must have uniform gain across its active area and for a range of angles determined by the input optics. The gain must be stable and fast enough to allow eventual optical processing techniques to be competitive with similar digital processing techniques. Finally it would be desireable to have the gain function introduce only a uniform phase to the input optical wave so that the output field is temporally and spatially coherent with the input.

Noise is the next important factor in the usefulness of an optical amplifier. The useful dynamic range of an amplifier is determined by the maximum output signal level and the output noise. One measure of dynamic range is the ratio of the maximum output to the minimum output where the minimum output is usually considered to be when the signal is equal to the noise. A good amplifier is one which amplifies only the noise already present in the image and does not add its own noise. Sources of noise in a light amplifier could include scattering off of optical surfaces, scattering of the pump beam from imperfections in the crystal and background light.

This chapter will analyze $BaTiO_3$ for use as an optical amplifier. A crystal of $BaTiO_3$ will be characterized through measurements and expressed in terms of the theoretical equations developed on Chapter II. The primary source of noise, pump beam scatter, will also be characterized through measurements. The relationship between the crystal gain coefficient, pump scatter, and beam fanning will then be presented with the resulting impact on optical amplifier performance. With this relationship a method for optimizing $BaTiO_3$ for image amplification will be presented and an optimum configuration for a specific crystal will be proposed. Finally an evaluation of the crystal will be made when put into this configuration.

3.2 Optical Gain in BaTiO₃

Optical gain in BaTiO₃ is the result of the holographic diffraction of energy from a pump (or reference) beam into the direction of a signal beam. Since the spatial shift of the holographic grating is $\pi/2$ relative to the intensity peaks of the pump and signal beam interference pattern, the light diffracted from the pump beam is in phase with the light in the signal beam and they add coherently. For the same reason, light diffracted from the signal beam into the direction of the pump beam coherently subtracts from the pump beam's intensity. The differential equations for describing this process (2.35, 2.36, 2.38, 2.39) were derived in Chapter 2. Time and crystal absorption will not be considered, since all measurements will be made after steady state has been reached and the calculations for gain will cancel out the absorption factor.

The experimental set-up used to collect two-beam coupling data is shown in Figure 3.2. A coherent INNOVA 100-20 Argon Ion laser with an internal etalon is used to produce single longitudinal mode light at 514.5 nm. Three devices are used to control the beams before they entered the crystal. A continuously variable attenuator (CVA) is used to precisely control the argon laser output. During experiments, the laser output power can also be stabilized by placing it into a constant output mode and it will keep a constant output power by automatically adjusting the laser tube current. The polarization rotator (PR) is used for setting the polarization to horizontal for extraordinary and vertical for ordinary polarizations. A spatial filter/collimator (SFC) is used to expand and collimate the laser beam to a 2 inch diameter. This also assures a uniform pump beam intensity.

The expanded beam is split into two beams with a 50/50 beam splitter (BS). The pump beam is taken to be the one transmitted through the beam splitter. Aperture 1 is used to restrict the size of the pump beam entering the crystal. The beam reflected from the beam splitter serves as the signal beam and is passed through neutral density filters (NDF) and a circular variable attenuator. The neutral density
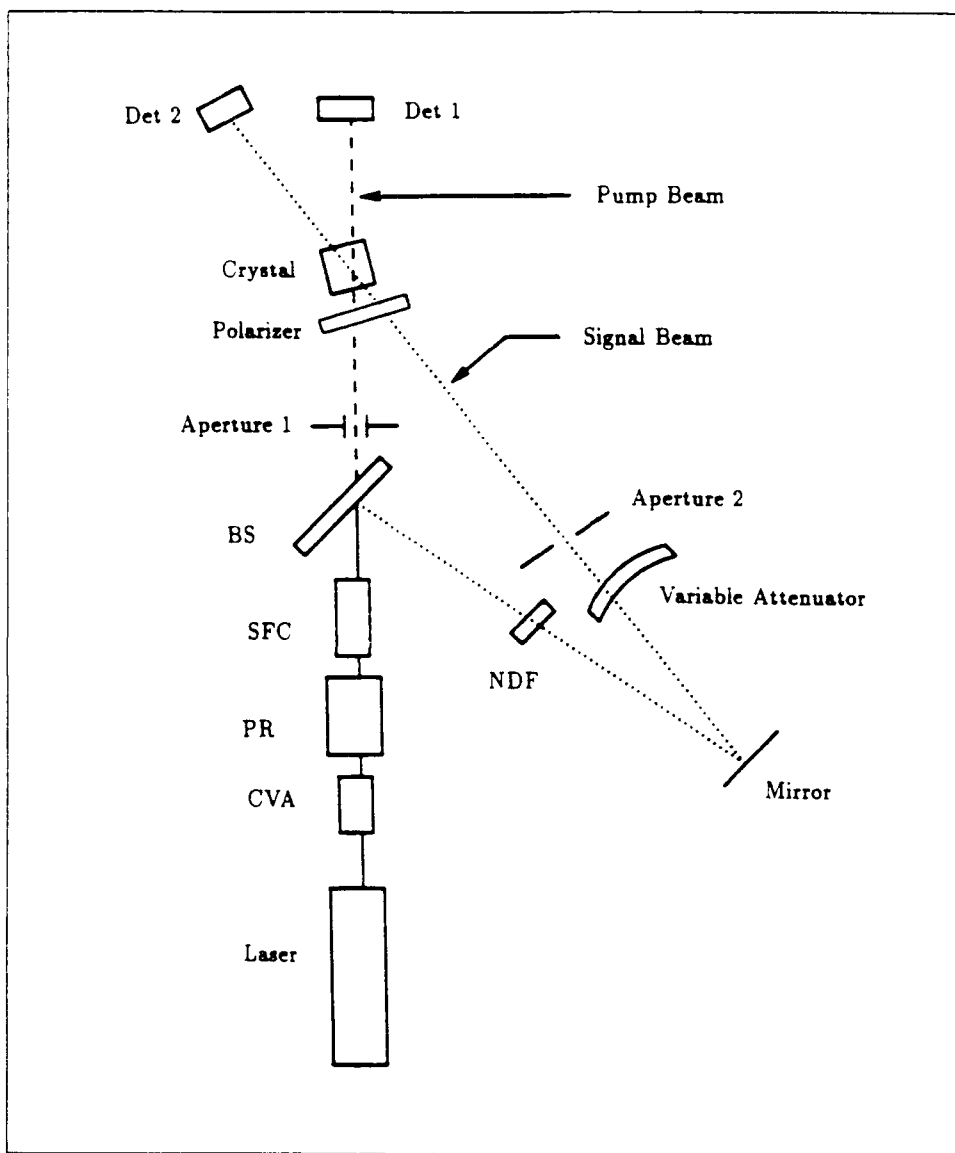
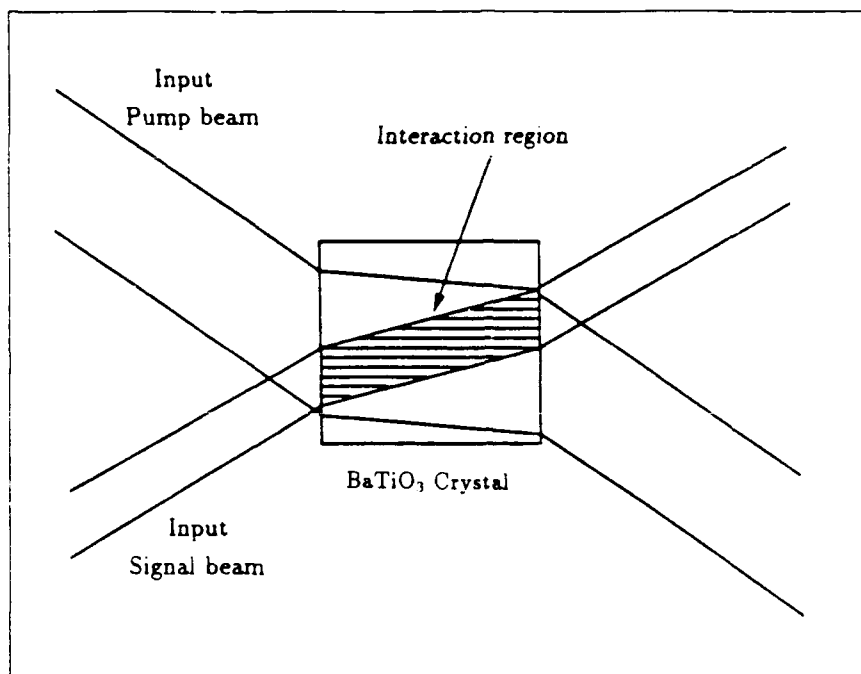Figure 3.2. Two-Beam Coupling Experimental Set-up

Figure 3.3. Pump and Signal Beams Inside the Crystal

filters are required since the circular variable attenuator only has a dynamic range of 100/1. Aperture 2 is then used to restrict the size of the signal beam to assure complete overlap by the pump beam. This condition is shown in Figure 3.3 and is important since all parts of the signal beam must be in the pump beam for uniform gain across the signal beam. Both apertures are adjusted so that the beams enter and leave the crystal without touching a corner or side. This is important since light scattered from the corners and edges can also be amplified by the pump beam, thus competing with the signal beam for pump power. Before either beam enters the crystal, a polarizer is used to guarantee the proper polarization since the coated mirrors and beam splitter can rotate the polarization by up to 5° as well as make it elliptical. The cross polarization extinction ratio of the polarizer is better than 100/1. Detectors, Det 1 and Det 2, are used to measure the transmitted pump and signal beam intensities respectively.

The gain measurements are made with Newport 835 optical power meters us-

ing Newport Model 818-SL detector heads. The dark cell noise for this equipment is 3 nanowatts. An aperture with a 3mm diameter is placed over the detector's entrance to minimize room background noise which, with the laser on, is typically 10-90 nanowatts. During each experiment the signal beam power is measured before the pump was applied $P_s(L)^-$ and after the pump beam is applied $P_s(L)^+$. The input signal beam is then removed and its grating is allowed to die out with the pump still applied to get a measurement of the beam fanning noise $P_n(L)^+$. The L in these expressions signifies that the measurement is taken after the beams propagated through thickness L of the crystal. A 0 instead of an L would signify that the measurement is taken before the beam passes through the crystal. The superscript + and − identify whether the pump beam is 'on' or 'off' respectively. The corresponding signal and pump intensities, called I_s and I_p respectively, are found by dividing the power by the appropriate beam areas, defined by 2mm and 4mm diameter apertures respectively.

The intensity gain G is calculated by the formula

$$G = \frac{P_s(L)^+ - P_n(L)^+}{P_s(L)^-} \tag{3.2}$$

where the beam's power can be used in place of its intensity since intensity and power are proportional by the beam's cross sectional area. Even though the signal and noise beams are temporally coherent, their powers are subtracted as if they are incoherent. This is justified since they are spatially incoherent over the detector aperture due to the random nature of the fanning generation (see the next section on beam fanning). The use of output signal powers with and without the pump beam separates gain effects resulting from the two-beam mixing from the transmission losses through the crystal due to reflections from the faces and the absorption losses within the crystal. These losses will result in an input/output gain which is less than the theoretical gain in an actual optical amplifier implementation. Care is taken to assure that $I_s(L)^+ \ll I_p(L)$ so that the amplifier is not saturated.
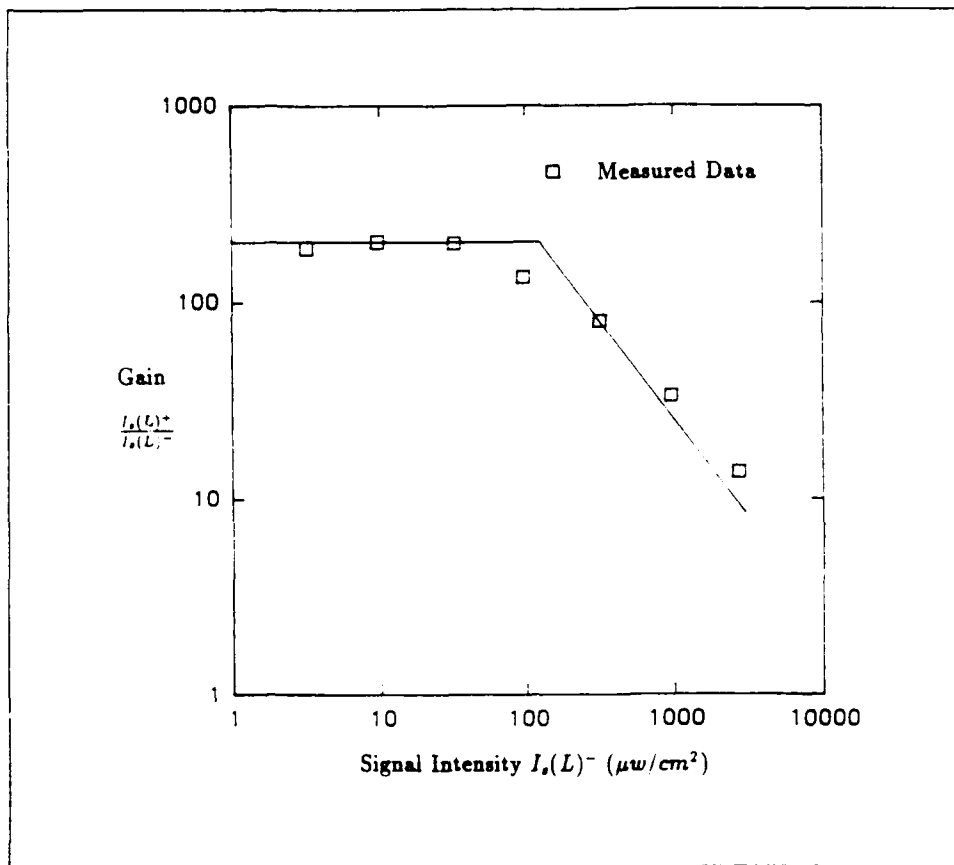
Figure 3.4. Typical BaTiO$_3$ Crystal Steady State Gain Measurement as a Function of Input Signal Intensity

3.2.1 Small Signal Gain Measurements. Figure 3.4 shows the result of a two-beam mixing experiment in which θ, β, and I_p are held fixed and the output signal intensity gain is plotted as a function of input signal intensity. Notice that the shape of this curve is the same as the theoretical curve shown in Figure 2.4 in Chapter II. This figure demonstrates that the crystal signal gain G is independent of pump and signal beam power until the amplified signal beam's intensity approaches that of the pump beam's intensity. The " knee " in the curve is where this occurs. For input signal beam intensities higher than this point the output signal intensity is limited to a value proportional to the pump beam's intensity. From Figure 3.4 the output signal beam intensity would have been 24 mw/cm^2 if the gain had remained constant out to the knee. As was expected this is close to the 35 mw/cm^2 of the pump beam

intensity.

The gain coefficient for this configuration can be calculated using Equation 2.39 assuming $I_s(0)e^{\Gamma\zeta_s} \ll I_p(0)$, and letting $\zeta_s = L$.

$$\Gamma = \frac{1}{L}\ln G_{ss} \qquad (3.3)$$

where G_{ss} is the small signal gain and is defined as the gain in Figure 3.4 where the curve is horizontal and the gain is constant with respect to input signal level. An $L = 5.0\text{mm}$ results in a $\Gamma = 1.05/\text{mm}$ for the crystal conditions in this figure.

3.2.2 Characterizing the Gain of a BaTiO₃ Crystal for use as an Optical Amplifier. The two-beam coupling gain of a particular sample of $BaTiO_3$ is determined by its gain coefficient and the crystal's thickness. The basic physics of the photorefractive effect is well understood and has already been described. The exact identity of the photorefractive sources and traps, however, remains unclear [25, 26]. This lack of understanding, therefore, hinders the control and optimization of $BaTiO_3$'s nonlinear-optical and photorefractive properties. Thus crystals, grown under apparently the same conditions, could have significantly different characteristics due to small differences in feed material purity or subtle differences in procedure. It is for this reason that each crystal must be characterized before it is used as an optical amplifier.

Two-beam coupling data for characterizing $BaTiO_3$ crystals is typically taken using extraordinary polarization, for $\beta = 0$, and varying θ [25]. The data is then used to determine the effective density of empty traps N_E involved in the photorefractive process as well as a correction factor to the effective electro-optic coefficient. The first of these parameters is $N_E = N_A(1 - N_A/N_D)$. The second and third parameters are used to produce a corrected effective electro-optic coefficient $R'_{eff} = F_p\bar{\sigma}R_{eff}$ where F_p is the fractional poling and $\bar{\sigma}$ is the normalized differential conductivity.

The latter term is defined by

$$\bar{\sigma} = \frac{\mu_n p_{holes} - \mu_e n_{electrons}}{\mu_n p_{holes} + \mu_e n_{electrons}} \tag{3.4}$$

where μ_h and μ_c are hole and electron mobilities and p_{holes} and $n_{electrons}$ are hole and electron number densities. $\bar{\sigma}$ thus accounts for electron-hole competition and the sign/direction of the c-axis. It is not uncommon for the sign of the dominant carrier to be different between crystals resulting in a difference in the direction of two-beam coupling gain relative to the crystal poling direction. The factors $F_p \bar{\sigma}$ and N_E are thus used to modify the theoretical equations to give the best fit to the data.

Figure 3.5 shows an example of data gathered on BaTiO$_3$ crystal #164-E using extraordinary polarization, where θ has been kept constant and β has been varied. This form of measurement is preferable over the method identified in the previous paragraph, since the crystal is simply rotated, requiring little or no beam readjustment. Also, since multiple reflections within a crystal sometimes give an erroneous reading, rapid changes in gain for small changes in β can filter these conditions out. This also avoids the problem of errors created by readjusting the beams' overlap for each new θ since measurements made early in this effort and reported by Keppler [15] showed that crystal gain could vary by as much as 50% by using different parts of the same crystal. Based upon the data shown in Figure 3.5, $F_p \bar{\sigma} = 1$ and $N_E = 2.4 \times 10^{16}/cm^3$ for BaTiO$_3$ crystal #163-E.

The exponential gain coefficient for BaTiO$_3$ crystal #164-E can now be calculated and expressed as a function of β and θ. Using $F_p \sigma$, N_E, $E_0 = 0$, and $u = 0$, Equation 2.37 for Γ is shown in Figure 3.6 as a three-dimensional plot for all possible β and θ. From this plot it can be seen that there is a positive symmetry about $\beta = 0$ and a negative symmetry about $\theta = 0$. A negative Γ indicates that the pump beam is amplified at the expense of the signal beam. There is only a small range of β and θ where the gain coefficient is very large.
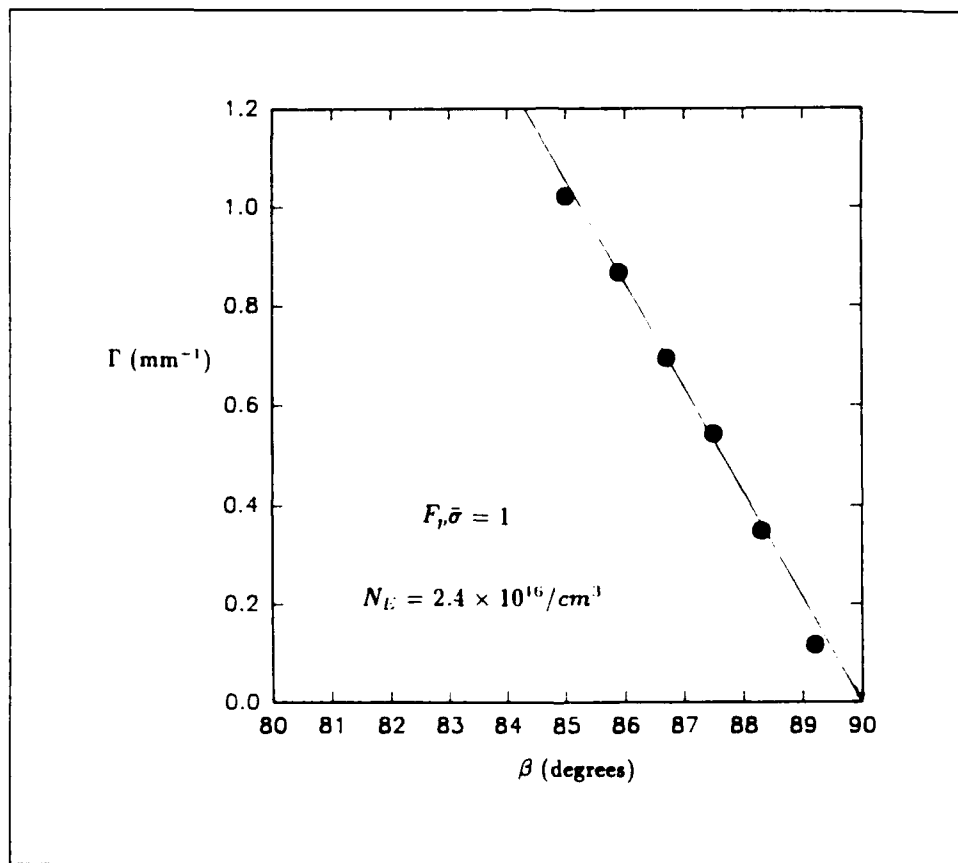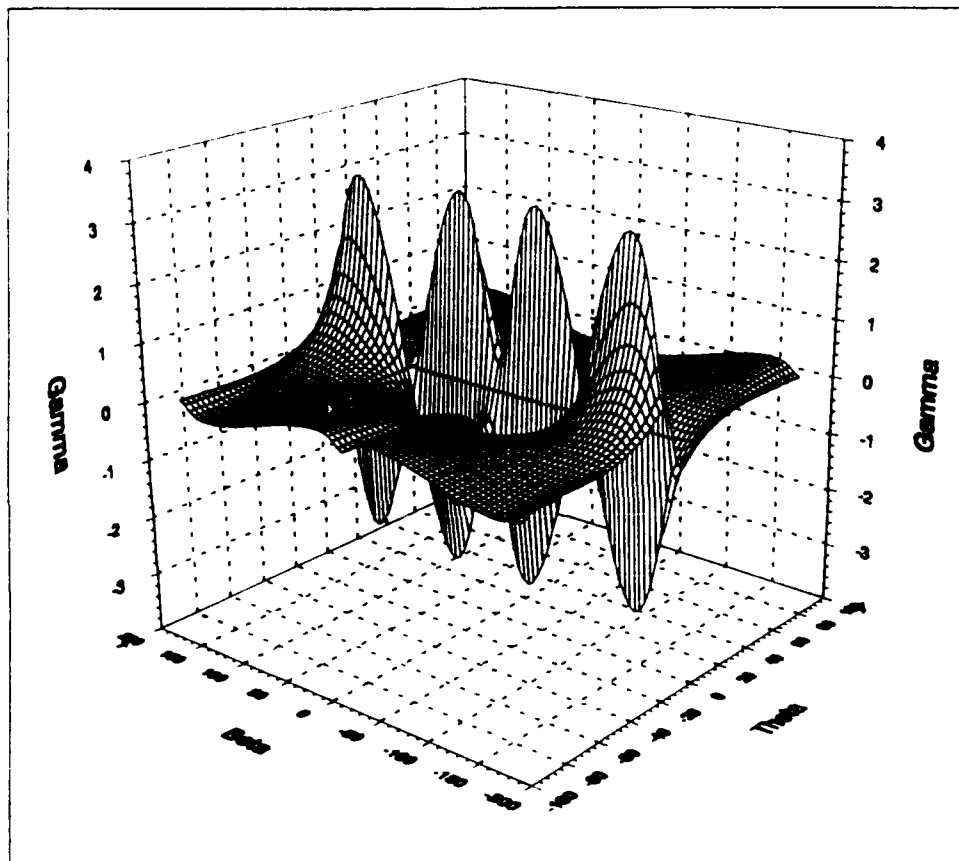
Figure 3.5. Two-Beam Coupling Gain Coefficient Measurements

Figure 3.6. Three Dimensional Plot of Γ as a Function of β and θ

The final measurement which is required to characterize the BaTiO$_3$ crystal is its reflection and transmission losses. The absorption coefficient α is calculated from the measured transmission T according to

$$\alpha = [2\ln(1 - R) - \ln T]/L \qquad (3.5)$$

where R is the reflectance and is related to the refractive index by

$$R = (n - 1)^2/(n + 1)^2 \qquad (3.6)$$

for the case of normal incidence. The appropriate refractive index n is used for the light's wavelength and polarization. For the crystal measured in Figure 3.5 $T = 0.44$, $R = 0.173$, $\alpha = 0.088/mm$ for extraordinary polarization at 514 nm. The transmission losses are exceptionally high due to the large refractive index of the BaTiO$_3$. It is possible to reduce these losses through the use of anti-reflection coatings.

3.3 Noise Sources in BaTiO$_3$

When a weak coherent optical signal is passed through a BaTiO$_3$ crystal being illuminated with a strong pump beam at the same frequency, it experiences gain through the two-beam coupling process. As with all amplifiers, the presence of noise sources will add to and corrupt the quality of the emerging amplified optical signal. This problem is particularly disturbing for low-intensity injected signals and contributes to poor signal-to-noise ratios in the detection plane. In photorefractive amplifiers the spontaneous optical noise emission and amplification (commonly referred to as beam fanning) originates from coherent light scattered in, or reflected from, the crystal imperfections and interfaces. A portion of this light propagates in the same direction as the injected signal and is also amplified through the formation of parasite noise gratings with the pump beam. Furthermore, the maxima of noise power obviously occur along the directions of maximum gain, making it difficult to suppress the noise of the photorefractive amplifier efficiently while maintaining high
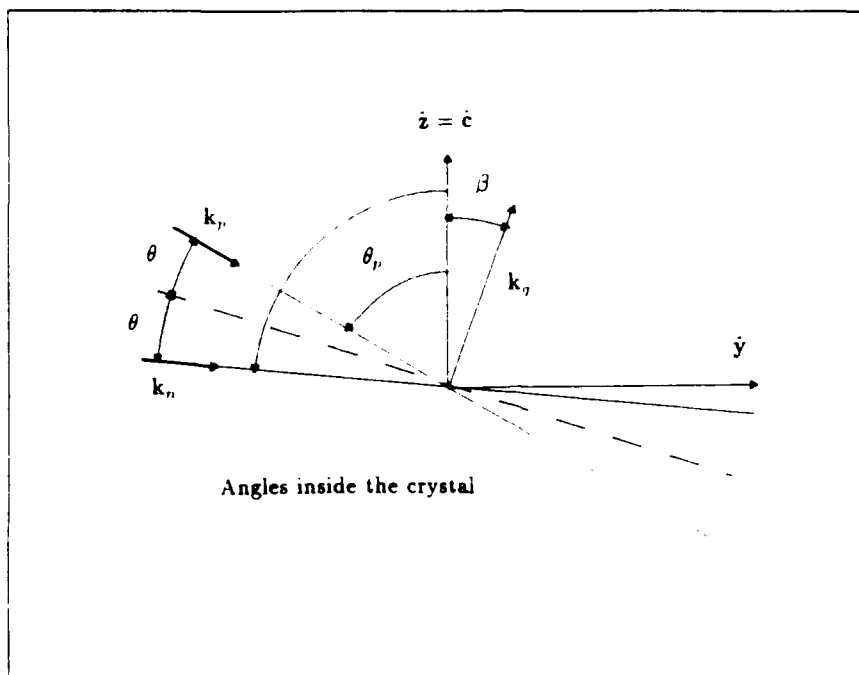
Figure 3.7. Angle Definitions for Beam Fanning

gain for the signal [23]. The problem is further compounded for high gain config-
urations when the noise, which initially is negligible in intensity, can grow until it
significantly depletes the pump beam [24]. This latter problem results in a reduction
in the measured optical gain for high gain configurations [11].

3.3.1 Beam Fanning Geometry The amount of beam fanning and two-beam
coupling gain is very dependent upon the angle which the pump beam makes with
the c-axis. Referring to Figure 3.7, the pump beam with wave vector k_p makes an
angle θ_p with respect to the crystal c-axis. Scatter from imperfections in the crystal
generate random noise rays of light in $\hat{k}_n$ directions, each of which makes a different
angle 2θ with respect to k_p. The following discussion considers only rays in the $\hat{c}$ -
k_p plane, since they will be the ones generating fanning power which competes with
the signal beam, also in this plane. Analysis will be performed later to include a
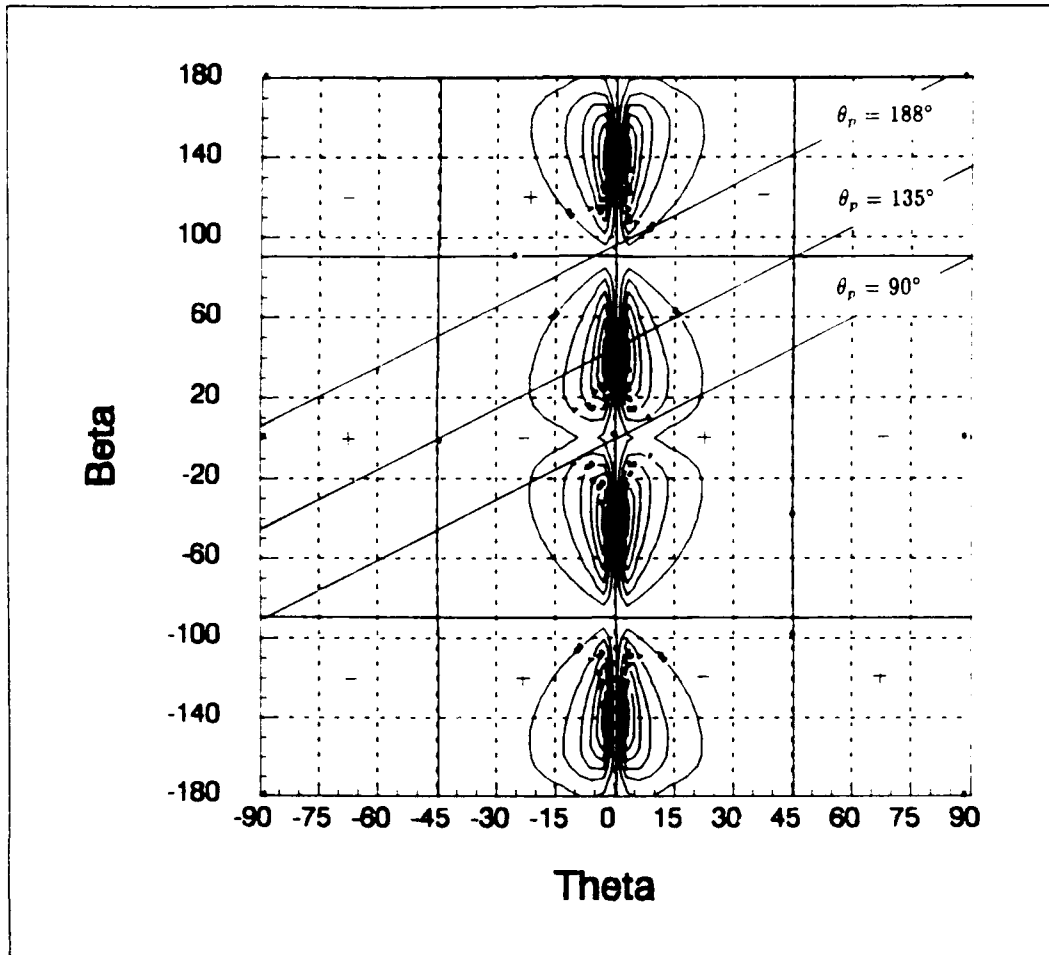more general k_n. The scattered light can be in all directions with $-90° < \theta \leq 90°$.

3-14

Figure 3.8. Contour Plot of Gain Coefficient as a Function of β and θ

Each grating resulting from the pump and a scattered light ray at 2θ has a β where

$$\beta = \theta_p + \theta - 90° \tag{3.7}$$

What this means in terms of the possible crystal gains accessible is shown in Figure 3.8. This figure is a contour plot of Figure 3.6 for equal Γ's and all possible θ and β. The diagonal lines on the plot represent three pump beam/c-axis conditions and the resulting (β, θ) points possible from Equation 3.7. It is worth noting that these same diagonal lines also represent the range of signal beam possibilities, since noise in the same direction as the signal realizes the same amplification.

3-15

3.3.2 Crystal Scattering Measurements The crystal scattering measurements were made at the same time as the gain measurements. Once G was determined it was then used to calculate the intensity of the scattering noise at the input face of the crystal by dividing it into the fanning noise intensity at the output

$$I_n(0)^+ = \frac{I_n(L)^+}{G}$$

Since this noise was the result of scatter from the pump beam, it can be normalized by the pump power to give a fractional power scattered into the signal beam direction. For crystal #164-E, whose gain measurements were given in the previous section, this fractional scatter η_{scat} was found to be 0.1 - 1.0 $\times 10^{-6}$ where

$$\eta_{scat} = \frac{I_n(0)^+}{I_p(0)} \tag{3.8}$$

3.3.3 Optical Gain and Beam Fanning Since beam fanning is the result of amplified light scattered from the pump beam, it is reasonable to expect that the pattern of the fanning can be calculated based upon the pump beam and crystal orientations. As stated earlier, pump beam light can be scattered from either crystal interfaces or defects in the crystal lattice. Examples of scatter from an interface include dust, scratches, or finger prints on the faces of the crystal. Examples of defects in the crystal could include lattice vacancies, material impurities, or inclusions. The latter defect, inclusions, is a term given to crystal defects associated with the crystal growth in which the crystal component concentrations are nonuniform. For the purpose of calculation it is assumed that all of these scatter sources are small and random with uniform distribution over both the crystal volume and the angles which will exit the crystal output face. Observations of the scattered light by imaging the crystal output face onto a CCD TV camera verifies the random spatial distribution of the light and can be seen in Figure 3.9. By placing a polarizer between the crystal and TV it can be shown that the scattered light is polarized the same as the pump beam. A measurement of the cross polarization component can not be made, however, since the camera does not have sufficient sensitivity to detect it.
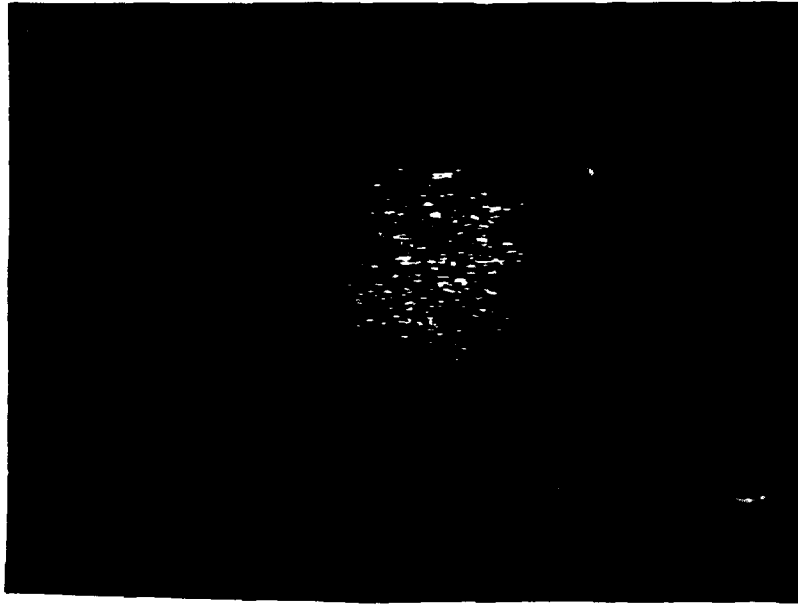
Figure 3.9: Scattered Light in the BaTiO$_3$ Crystal

The intent of this subsection is to demonstrate the relationship between pump beam input angle relative to the crystal c-axis and the resulting observed beam fanning pattern. This comparison is only approximately valid since the gain calculations are for angles inside the crystal and the beam fanning patterns are observed outside the crystal. It has been assumed that these patterns are linearly related using Snell's Law and the small angle approximation for the sine (9% error for an external angle of 45°).

A computer program was written for calculating two-beam mixing gain with arbitrary input pump and signal beam propagation vectors. This program is unique over other calculations in the literature in that it allows the signal beam's propagation vector to be out of the k_p - c-axis plane. Polar coordinates are used to describe a fixed k_p and a range of K_n directions. The equations developed in Chapter II for the extraordinary polarization condition are used for calculating the gain coefficient and an effective propagation length of 6mm is used to calculate two-beam gain. Three conditions were used for demonstrating the relationship between the crystal gain equations and the beam fanning pattern: Condition 1 - k_p and the c-axis

approximately parallel and in the same direction, Condition 2 - k_p and the c-axis parallel and in opposite directions, and Condition 3 - k_p and the c-axis perpendicular. The first two conditions were selected to keep the gain low enough so that the fanned energy was not saturated at the output causing a distortion in the fanned pattern. The last condition was selected since this condition is the one most commonly used when first testing a new $BaTiO_3$ crystal.

A three dimensional plot and a contour plot of the gains resulting from condition 1 is shown in Figures 3.10 and 3.11. Under this condition k_p and the c-axis are approximately parallel and in the same direction. The inset in the first figure shows this and the relationship between the polar coordinate system used to describe the pump and arbitrary noise (or signal) rays and its relationship to the Cartesian coordinate system describing the crystal and its c-axis. (Note that the θ used here and for the next two conditions is the general polar coordinate and is not related to the angle 2θ between the pump and signal beams.) This condition provided the most control for crystal gain in that the highest gain region was always between the pump beam direction and the c-axis direction. The amplitude of the gain was controlled by changing the angle between k_p and the c-axis. Larger angles produced larger gain. The shape of the fanning pattern is generally circular with the peak shifted toward the pump beam. The actual fanning pattern is shown in Figure 3.12. The bright square on the right is the pump beam after it has passed through the crystal. The fanning pattern is in the middle and the c-axis is shown as a white cross which has been added to show its approximate location. The rings in the fanning pattern which appear to be centered upon the c-axis are the result of an etalon effect caused by reflections of the scattered light from the front and back surfaces on the crystal.

A three dimensional plot and a contour plot of the gains resulting from Condition 2 is shown in Figures 3.13 and 3.14. Under this condition k_p and the c-axis are approximately parallel and in opposite directions. The inset in the first figure shows this and the relationship between the polar coordinate system used to describe
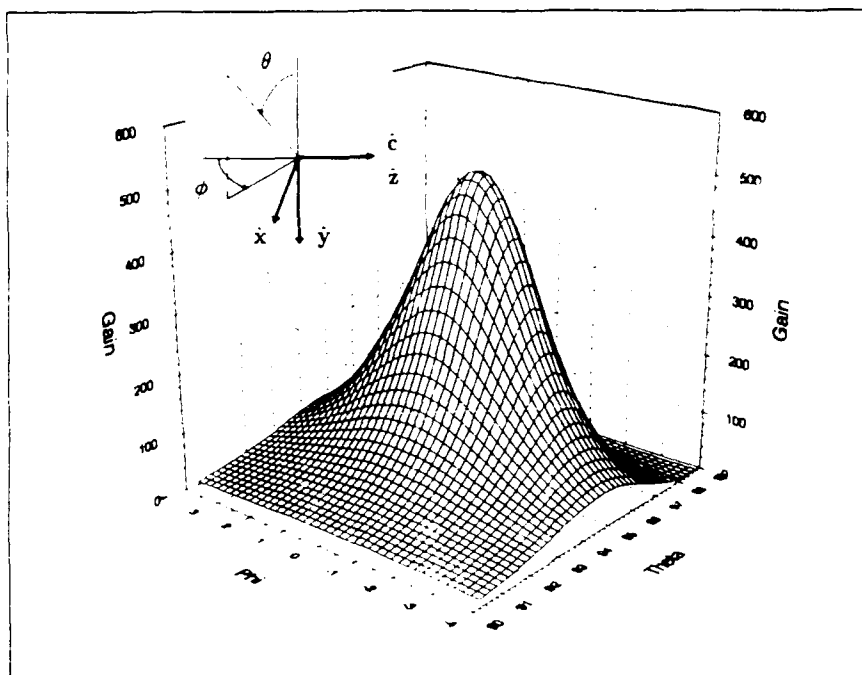
Figure 3.10. Three Dimensional Plot of Gain versus Input Angle for Condition 1
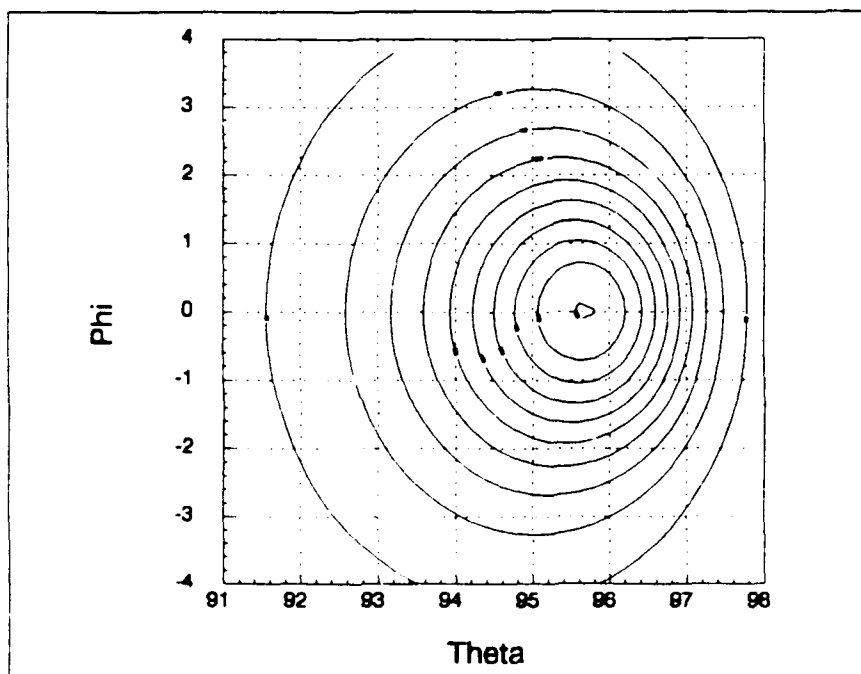

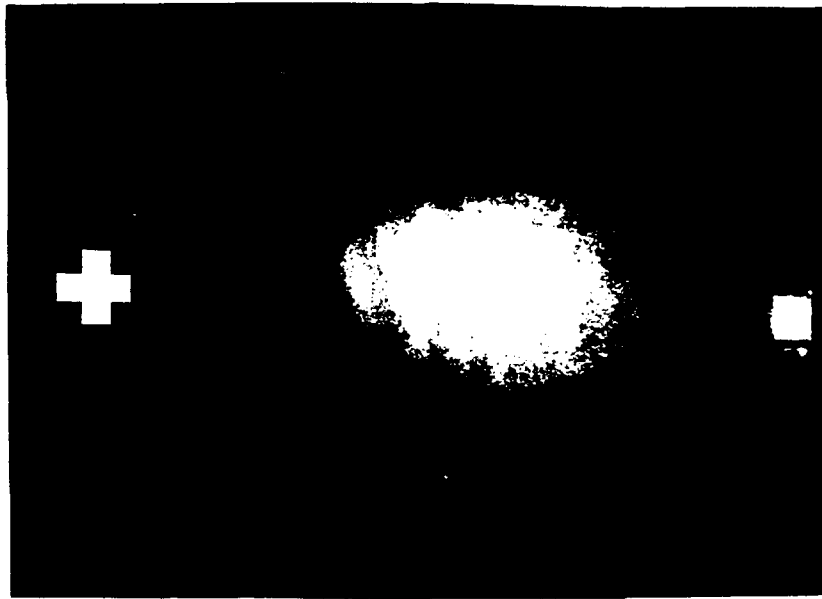Figure 3.11. Contour Plot of Gain versus Input Angle for Condition 1

Figure 3.12. Beam Fanning Pattern for Condition 1

the pump and arbitrary noise (or signal) rays and its relationship to the Cartesian coordinate system describing the crystal and its c-axis. The relationship between the polar and Cartiesian coordinate systems is different from condition 1 to allow linear variations in θ and ϕ to represent observed fanning patterns in the output. This condition proved to be harder to control since the gain becomes large for smaller variations in the angle between k_p and the c-axis. Also, since the high gain region is at an angle which is larger than the pump beam's relative to the c-axis, a runaway effect is produced. As pump beam energy is coupled into the high gain region, this energy behaves like a second pump beam which makes a larger angle with the c-axis. This larger pump angle produces a larger gain for noise at larger angles and is quickly coupled to them. The end result is the coupling of all pump energy away from its original direction. This can be observed in the crystal by an apparent bending of the pump beam as it passes through the crystal. This effect can be so strong that for a high gain crystal a pump beam propagating in exactly the opposite direction of the c-axis will appear to be split in half and curve to opposite faces before it reaches the output crystal face.
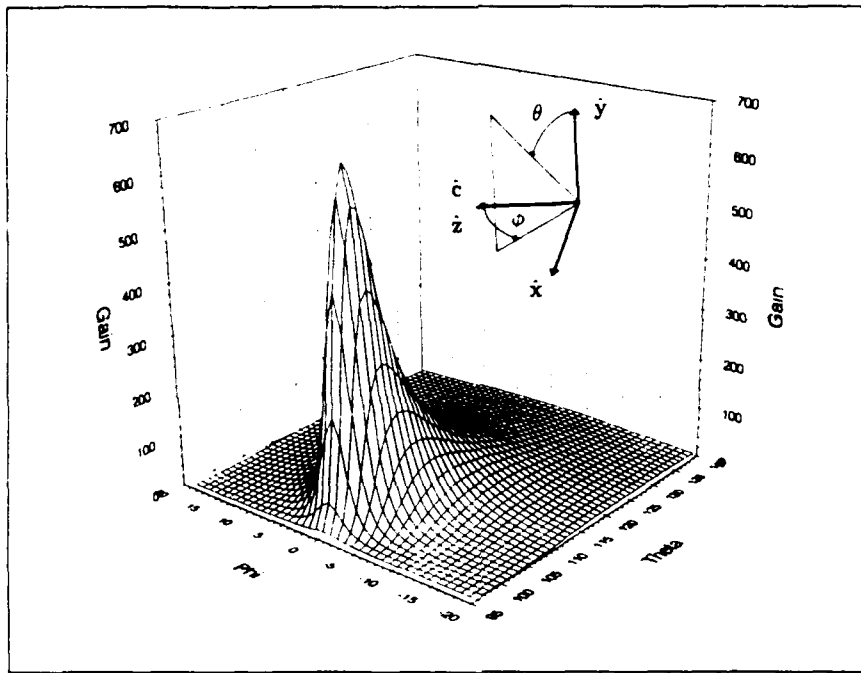
Figure 3.13. Three Dimensional Plot of Gain versus Input Angle for Condition 2
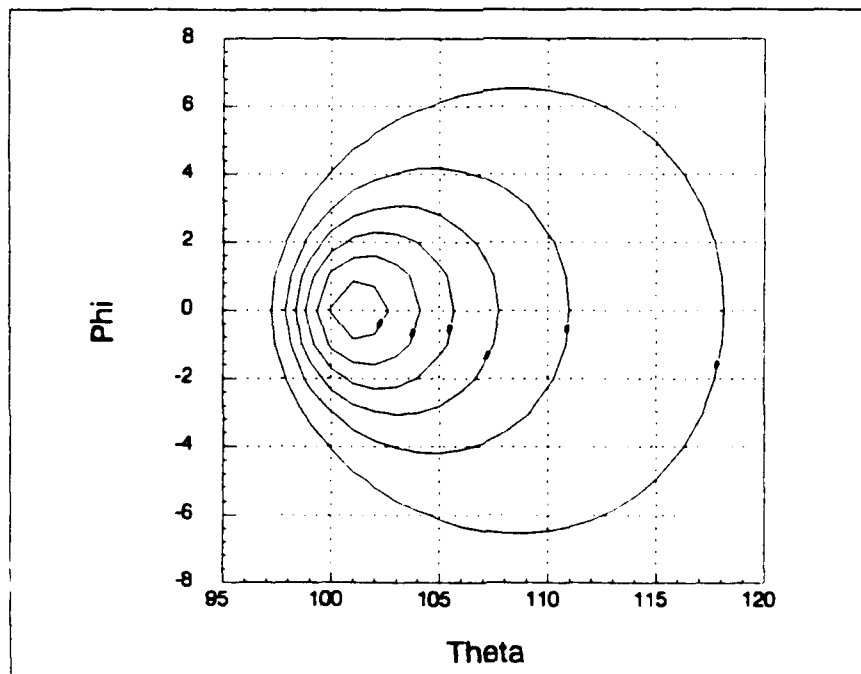

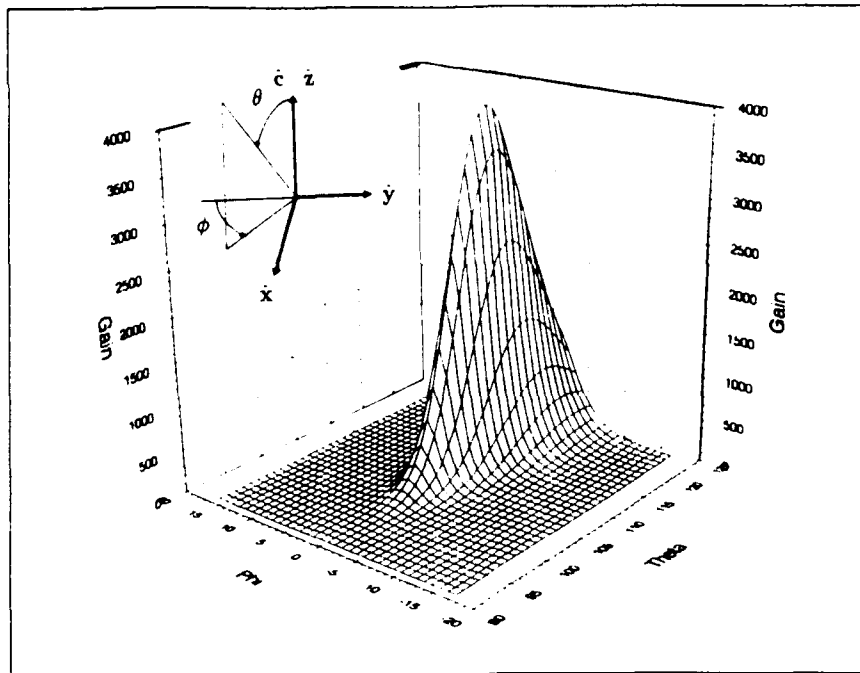Figure 3.14. Contour Plot of Gain versus Input Angle for Condition 2

Figure 3.15. Three Dimensional Plot of Gain versus Input Angle for Condition 3

A three dimensional plot and a contour plot of the gains resulting from Condition 3 is shown in Figures 3.15 and 3.16. Under this condition k_p and the c-axis are perpendicular. The inset in the first figure shows the relationship between the beam and crystal coordinate systems. As can be seen, the gain for this condition is very much higher than in the previous conditions. The fanning pattern would appear as a band of light increasing in intensity as it goes away from the k_p direction and into the c-axis direction. The peak of the fanning cannot be observed, however, since the light exiting the crystal in skewed by Snell's Law until it reaches the critical angle ($24°$, $\theta = 114°$ for this geometry) at which point the energy is totally reflected internally and exits some other face. Figure 3.17 shows this fanning pattern as a narrow, horizontal band of light going to the right from the central bright spot which is the direct pump beam. The fanning pattern producing a wing-like shape cannot be explained by the crystal gain equations. This effect is believed to be caused by defects in the crystal planes perpendicular to the c-axis. Further investigation is required to understand this effect.
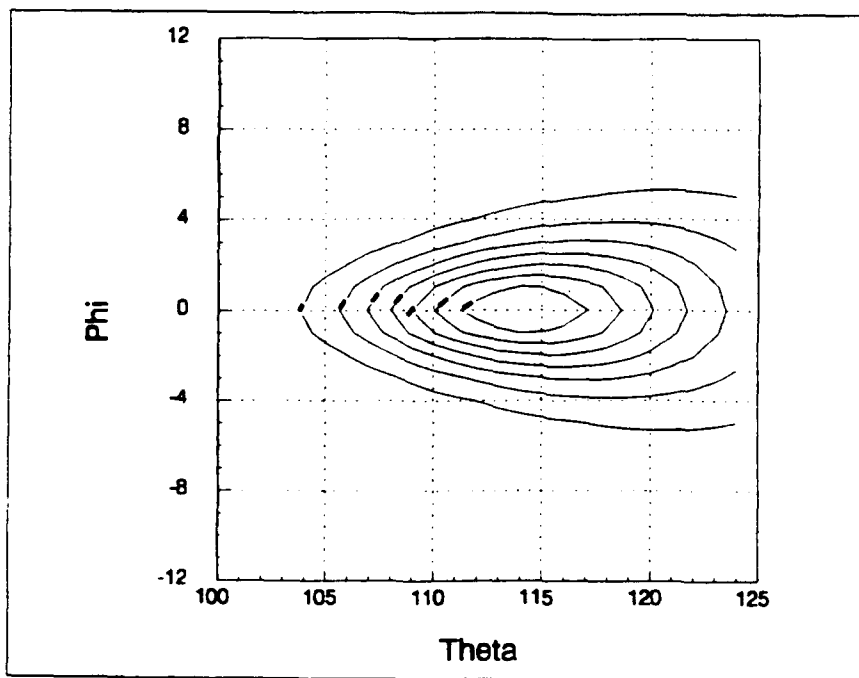
3-22

Figure 3.16. Contour Plot of Gain versus Input Angle for Condition 3

Figure 3.17. Beam Fanning Pattern for Condition 3

This subsection demonstrates the relationship between the crystal gain equations and beam fanning. It also suggests that the amount of beam fanning which will be observed can be controlled by selecting the proper pump beam and c-axis relationship. What was not stated, but should be obvious since the gain equations are the same, is that if a maximum signal beam gain condition is selected, it will also be in the peak of the beam fanning pattern. If the signal beam angles are not selected to give maximum gain for a given pump and c-axis orientation, then the noise will have a higher gain and extract more than its share of pump beam power. There is thus a direct relationship between the selection of optimized beam angles and beam fanning.

3.4   Optimizing BaTiO₃ for Image Amplification

3.4   Optimizing BaTiO$_3$ for Image Amplification

Although all of the desirable characteristics for BaTiO$_3$ have not been discussed, it is now possible to make a first cut at defining some of the more fundamental crystal characteristics. Measurements have been made which define a maximum output (saturation) intensity and characterize the crystal's gain coefficient and charge carriers. The dominant noise process which results from pump beam scattering has also been analyzed. The manner in which these characteristics determine an optimum optical amplifier is demonstrated in Figure 3.18 which shows a simplified relationship between the normalized signal output intensity and the crystal gain. The signal output is normalize o the pump signal since the pump's intensity sets the maximum level the amplified signal beam's intensity can achieve. The minimum input signal level is determined by the scattering coefficient of the crystal. This lower level represents the condition where the input signal beam intensity is equal to the intensity of light scattered from the pump beam. A signal, or noise, will saturate the amplifier if $e^{\Gamma L} = 1/\eta_{scat}$. The signal-to-noise ratio (S/N) of a amplifier is determined by the ratio of signal intensity to noise intensity at the output. Assuming that the signal and noise undergo the same amplification process and there are no
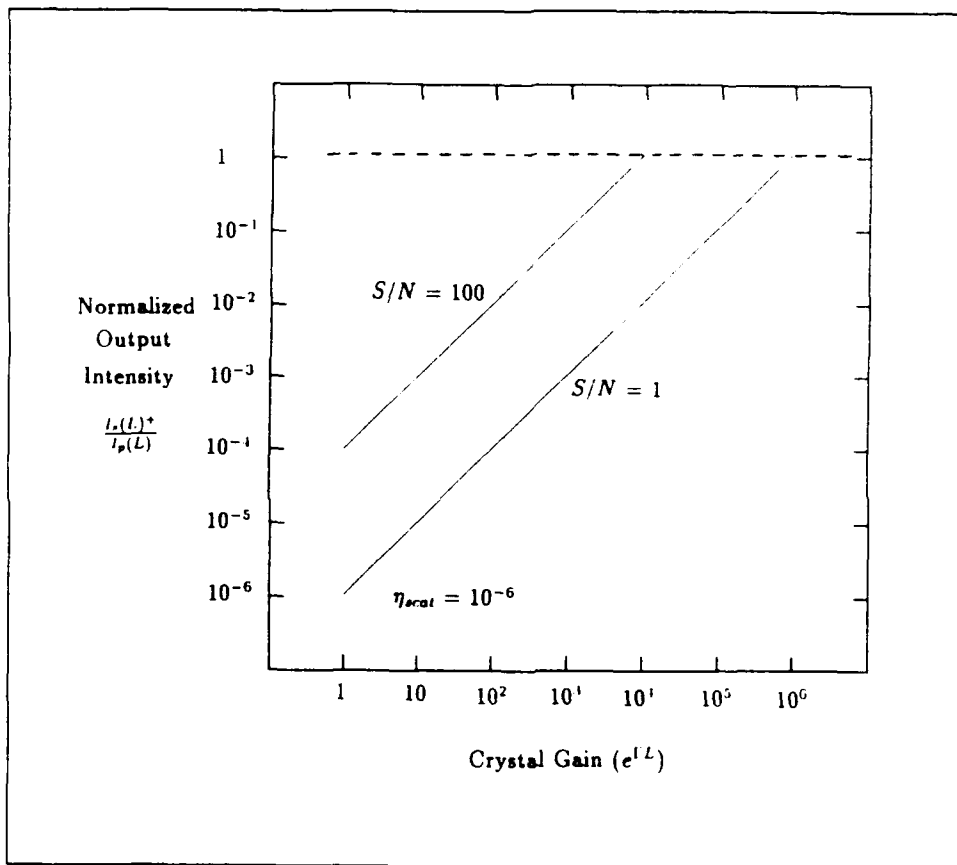
Figure 3.18. Normalized Output Intensity vs Crystal Gain

other noise sources, the S/N at the output is the same as the input. The maximum desirable crystal gain is determined when the signal output begins to saturate, since any additional gain will result in a decrease in S/N. This is shown in the figure for $e^{\Gamma L} = 10^4$ and S/N = 100. As long as the gain is below this saturation condition, the BaTiO$_3$ crystal behaves like a linear optical amplifier.

When specifying how an existing crystal is to be used, or when specifying a new crystal to cut, the parameters which can be varied are propagation length (approximately the crystal thickness) and Γ (a function of crystal cut and input beam angles). Based upon Figure 3.18 where $\eta_{scat} = 10^{-6}$ and the desired $S/N = 100$, the crystal gain should not exceed 10^4 or $\Gamma L = 9.2$. The optimum gain for an existing crystal can be established by controlling input beam angles and crystal orientation. The configuration which provides the most control is the first condition discussed in the previous section. By fixing the angle 2θ between the beams and varying β, the desired gain can be obtained. Selection of the angles is accomplished by using Figure 3.8 and selecting a θ_p line which just touches the $\Gamma = 1.5$ contour, where this particular Γ is selected since it gives $\Gamma L = 9.0$ for $L = 6mm$. Plotting Γ vs θ for a fixed θ_p results in Figure 3.19. From this figure Γ is maximum at $\theta = 1.8°$, thus establishing all of the required angles to achieve a signal gain and S/N. The required crystal orientation and beam angles are shown in Figure 3.20. This configuration as used in the following section for measuring image amplifier performance.

3.5 Image Amplifier Performance

Measurements on the crystal up to this point have been made with collimated beams and uniform intensity distributions across the crystal face. These measurements are necessary to characterize the crystal and verify the equations used to describe the two-beam gain process. This section looks at the crystal's performance as an image amplifier. Characteristics to be considered include gain, image resolution, noise sources, signal-to-noise, and dynamic range.
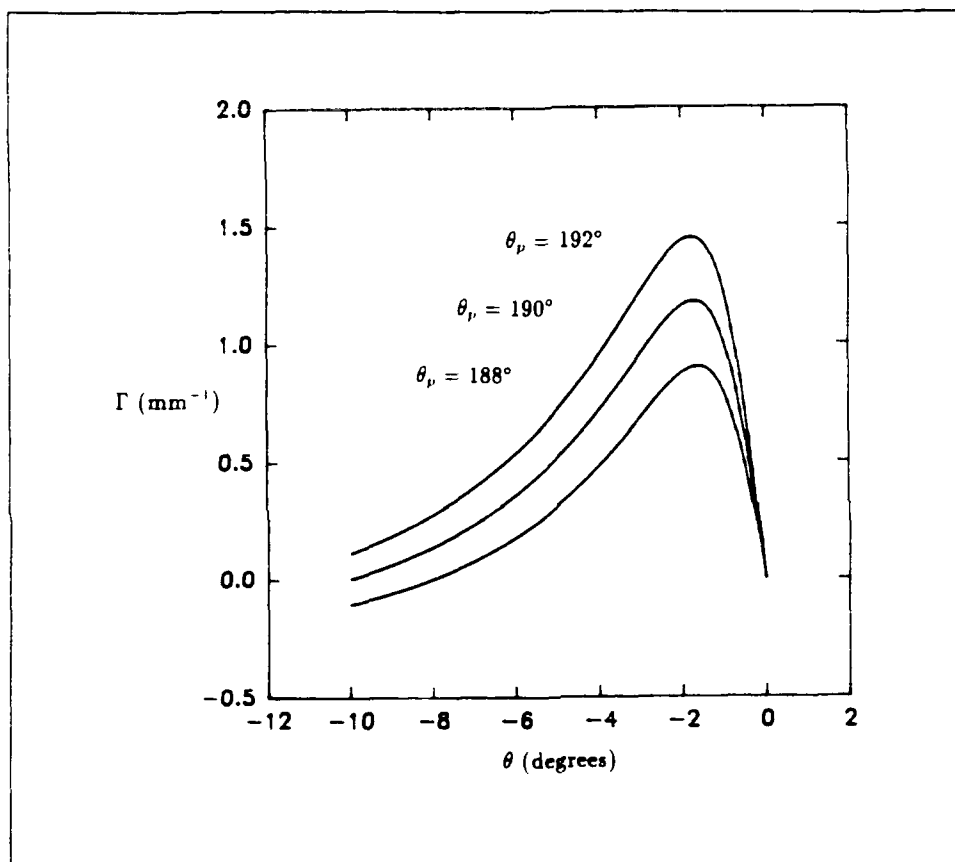
Figure 3.19.   Crystal Gain Coefficient as a Function of θ at the Optimum Pump Angle
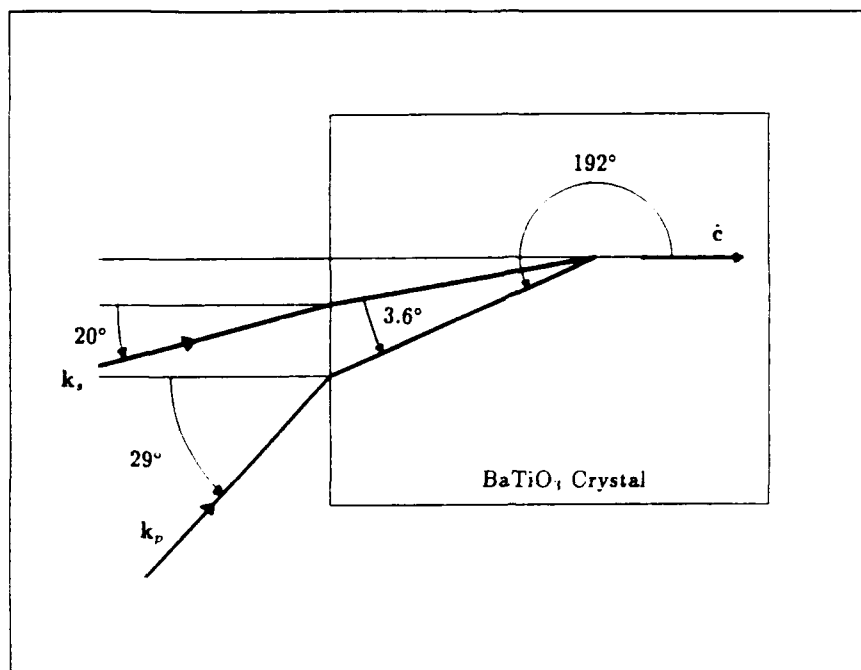
Figure 3.20. Optimum Pump and Signal Beam Angles for Crystal #164-E

The experimental setup is shown in Figure 3.21. The laser beam from the Argon Ion Laser is split into two beams by a 50/50 beam splitter (BS) to produce the pump and signal beams. Each beam path has a continuously variable attenuator (CVA) and a beam expander (BE). The signal beam is expanded to about 3 cm and passed through a resolution chart and iris. Lenses with focal lengths of 100 cm and 50 cm are used to minify and image the resolution chart onto the $BaTiO_3$ crystal. These long focal length lenses are used so that the feed back system described in the next chapter can be used with minimum setup changes. The pump beam is expanded to about 0.8 cm and passed through the crystal at an angle relative to the signal beam calculated to be optimum. Both irises are used to control the beam sizes at the crystal to ensure maximum use of the crystal volume without striking the sides and to assure complete overlap of the signal by the pump. The crystal is mounted upon a rotatable platform so that θ_p is easily varied. The amplified signal beam image is then reimaged upon a CCD TV camera for output analysis. A third iris is used before this last lens to minimize the light from beam fanning which would also
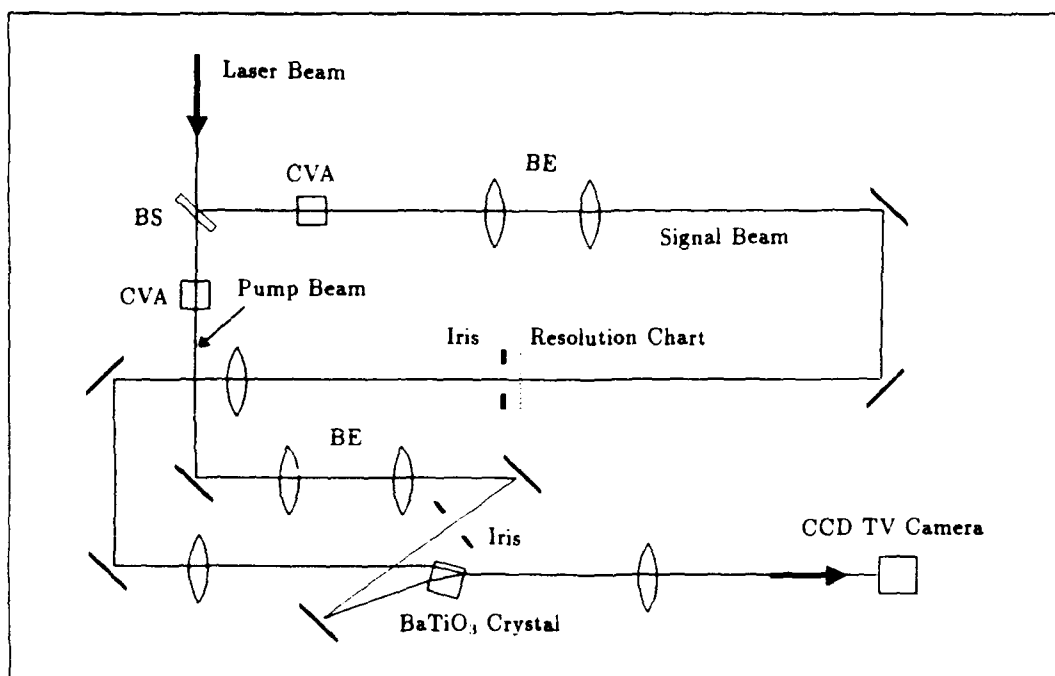
Figure 3.21. Experimental Setup for Measuring Image Amplification

be reimaged upon the TV. The size of this iris is selected to match the F-number of the input optics so as to match the input image spatial frequency content. The CCD camera is used as an imaging radiometer by calibrating its video output level as a function of input intensity. Calibrated neutral density filters are used to avoid saturation of the camera.

Figure 3.22 shows an image of the $BaTiO_3$ crystal as seen by the TV in the experimental setup. The polarized light reveals a number of interesting crystal properties. In this picture the c-axis is horizontal and going from right to left. The dark random spots appear to be caused by dirt on the crystal's faces. The vertical line in the crystal is along a crystal plane normal to the c-axis. Slight changes in the crystal angle will make this line dissapear. This crystal had only one such plane but others showed as many as a dozen. If the crystal is rotated so that the c-axis is toward the TV camera another inhomogenity can be observed. This characteristic appears to be a dark filament passing through the crystal parallel to the c-axis. Images passing
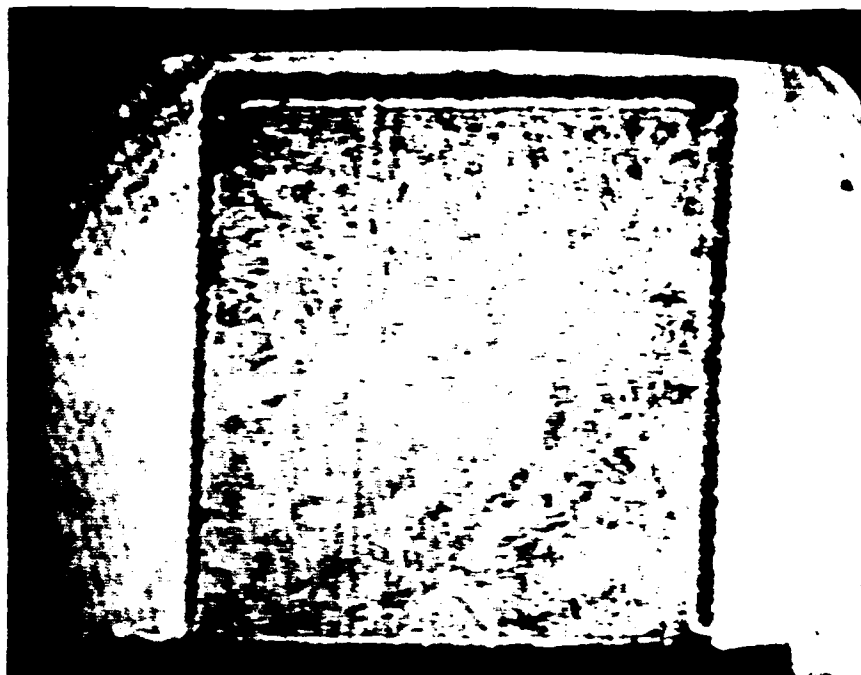
Figure 3.22. Image of BaTiO$_3$ Crystal

through these areas are slightly distorted.

By passing a strong pump beam through the crystal, light scattered into the signal beam direction can be observed. This is how Figure 3.9 was taken. The primary source of this light is dirt on the crystal face, which is verified by cleaning the crystal and observing an order of magnitude reduction in its level. The exact nature of scattering sources within the crystal, however, could not be identified. Measurement of the brightest noise points results in a scattering coefficient η_{scat} on the order of 10×10^{-6}. This number is higher than that measured before, since the earlier measurement was an average over the whole image.

The selection of the beam and crystal angles is made based upon earlier analysis. The angle between the c-axis and the pump beam θ_p is selected to be about 188° and the angle between the pump and signal beams $\theta_p - \theta_s$ is 1.5° to 2.0°. Since the gain is such a strong function of θ_p (G = 200 to 5,600 for θ_p = 188° to 192°) the final angle is selected by rotating the crystal until the amplified noise was 1/10 the pump

3-30
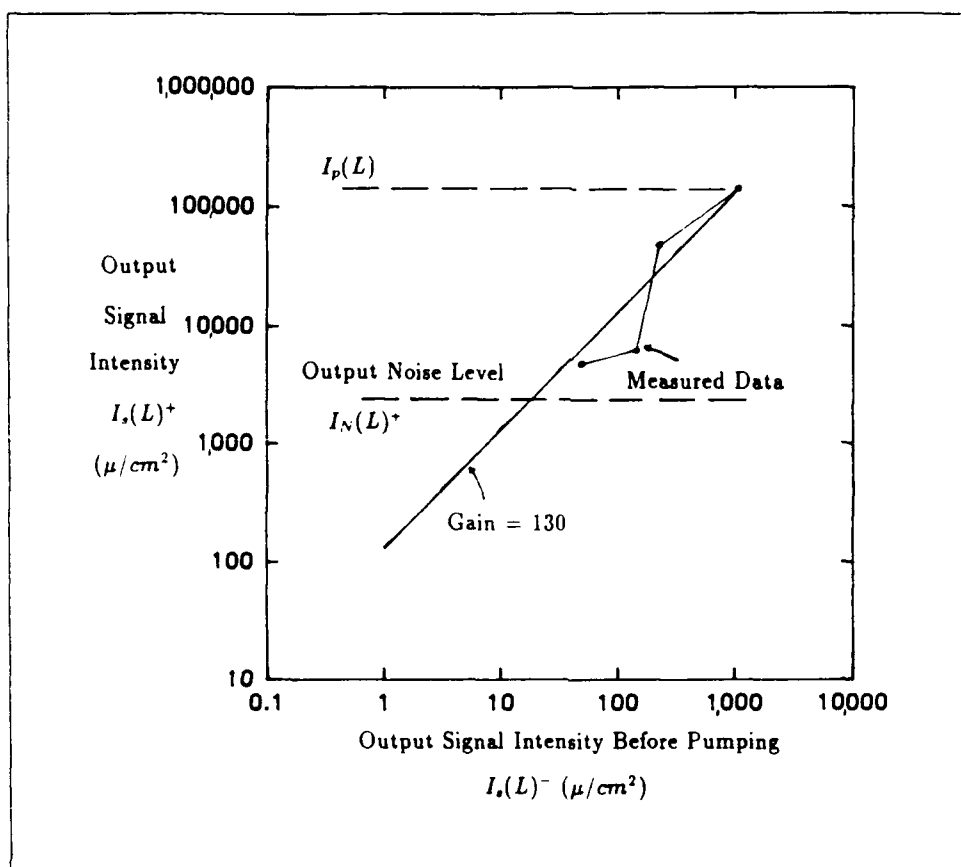
Figure 3.23. Image Gain Measurement Results

intensity. This would give the largest gain possible and still produce an output S/N = 10 for a nearly saturated signal. This angle was found to be 188 degrees.

Figure 3.23 shows the results of the measurements made for the above conditions. The pump beam intensity is shown as a horizontal line at 120 mw/cm². This represents a maximum amplifier output or saturation region. The peak output noise is shown at 3.5 mw/cm² and represents a minimum desirable signal output or a S/N = 1. A straight line has been drawn to represent the data if the crystal gain is 130 and to show how the data would look for a constant gain. Since the measured points do not lie on this or a parallel line, a problem with the data is identified. This problem is associated with the setup and results in low, unstable gains. Specifically the problem is due to a lack of stable coherence between the pump and signal beams

3-31
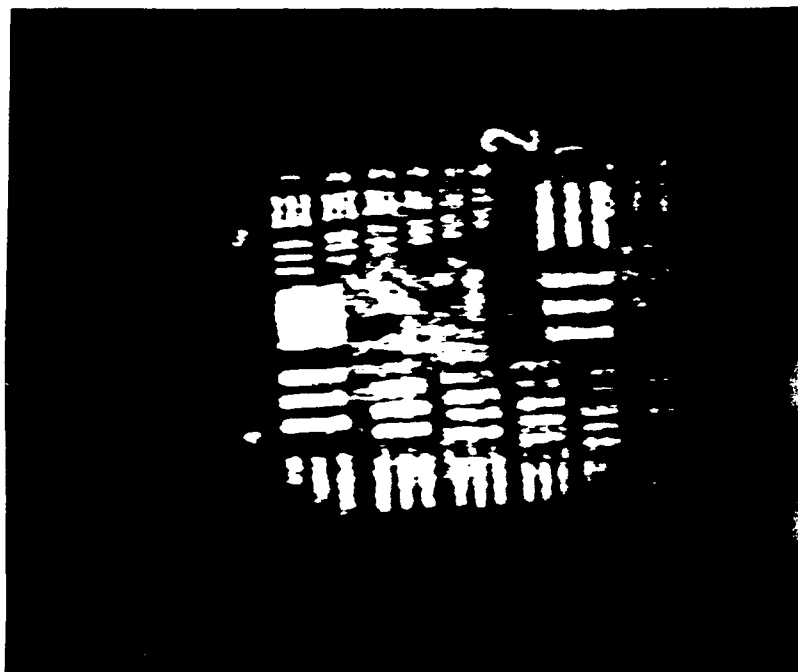
Figure 3.24. Example of Amplified Resolution Chart

caused by the long and different optical paths they take after being split from the main laser beam. Assuming a 1 meter path difference, a 0.1 C degrees temperature change, and a thermal coefficient of linear expansion for Iron of $1.19 \times 10^{-5}/C^\circ$ results in a path length change of 1.2 μm, or greater than two wavelengths of visible light. As an indication of what the gain should be, the noise intensity has been amplified by over 4,000 times. The noise does not have the same coherence/pathlength problem as the signal since the pump and noise beams are split at the crystal face.

Figure 3.24 shows another problem which is associated with reflections from the BaTiO$_3$ faces. The amplified signal image is specularly reflected from the output and input faces in sequence and generates a second, displaced image which competes with the first. The second image is displaced since the crystal's faces are not exactly parallel.

The resolution of the amplified image can also be seen in Figure 3.24. The third set of bars of the third group are spaced at 10 lines/mm. The input optics

to the crystal minify this image by a factor of two and thus results in 20 lines/mm in the crystal. This can be compared to the limiting resolution of the input optics which is 80 lines/mm.

The measured image gain and signal-to noise are both dissapointingly low. Rather than achieving a gain of 10^3 and a S/N of 100 the measured gain is only 1.3×10^2 with a S/N=10. The low gain is more of a problem with the setup, which requires long focal length lenses to control the input signal image. It does point out a practical problem which any application will also face in that care must be taken when planning pump and signal beam optical paths. The poor signal-to-noise is the result of using the peak noise intensity rather than the average.

Imagery of the crystal also identified possible flaws within the crystal which could affect amplifier resolution. The most significant improvement which could be made to a $BaTiO_3$ crystal is to carefully clean its input face since this will minimize the fanning noise and increase the allowable gain. A second improvement is to anti-reflection coat the input and output faces. This will increase the signal and pump throughput and minimize the double image problem associated with internal reflections.

3.6 Summary

The usefulness of $BaTiO_3$ as an image amplifier is determined by our understanding of the equations governing the two-beam mixing process. These equations, however, are ideal and do not fully take into account such things as fractional poling factor, normalized differential conductivity or pump beam fractional scatter. Since it is still not possible to manufacture these crystals to precise characteristics, it is thus necessary to characterize each crystal through measurements and curve fitting to model each crystal more precisely.

The dominant noise process in $BaTiO_3$ is beam fanning. Early researchers explained this process as the result of an index gradient caused by a nonuniform beam

intensity. Later research, however, showed it to be no more than the amplification of light scattered from the pump beam. For this reason the scattered light follows the same geometry rules as two-beam mixing. The beam fanning pattern is the result of relatively uniform scatter being amplified by an extremely nonlinear and geometry dependent process.

The trick to optimizing a $BaTiO_3$ crystal for an optimum gain condition is to specify a gain which is as large as possible, but not so large that the amplifier saturates from the input signal. Trying to achieve gains that are too high becomes counterproductive when the amplified noise is sufficient to saturate the amplifier, thus stealing energy from the pump beam. For this reason it is necessary to select a pump-to-signal angle which matches the peak in the beam fanning pattern. This then assures that there is not some other angle where the scattered pump light is saturating the amplifier. With this new-found understanding of $BaTiO_3$ it is now possible to talk about using it in practical applications.

IV. $BaTiO_3$ Optical Amplifier With Coherent Feedback

4.1 Introduction

The use of feedback in optical information processing is discussed in a review paper by Cederquist and Lee [4]. The meaning of the term "feedback" when applied to electronic circuits is well known: a portion of the (time-varying) output signal from a circuit is combined, often after modification, with the input signal and returned to the circuit. Electronic feedback is used to produce a unique (temporal) frequency response characteristic. When applied to an optical information processing system,"feedback" means that part of the output image (two-dimensional distribution of optical amplitude or intensity) is combined, again probably after modification, with the input image and thereby returned to the optical system. However, unlike electronic feedback, optical feedback is used to produce spatial (not temporal) frequency transfer characteristics which would be difficult or imposssble to achieve in other ways. Optical feedback can also be used to create nonlinear or space-variant optical processing systems.

The first steps toward the development of optical feedback were taken in the 1950's and 60's. Some good results were obtained, but it seems that little notice was taken of this early work. Widespread interest in the 70's began with the presentation in 1973 of experimental results showing the usefulness of optical feedback in image restoration, contrast control, and analog solution of partial differential equations. Several other methods for implementing optical feedback have been investigated experimentally since then. They can be classified according to the coherence length of the light sources used, ranging from long (single-mode lasers) through medium (multimode lasers) to short (incoherent light sources).

Lee and his co-workers at the University of California, San Diego (UCSD) continued to improve the techniques of coherent optical feedback into the early 80's [5].

In this work a confocal Fabry-Perot interferometer (CFPI) was used to produce feedback within an optical processor. The resulting confocal system had a complex-valued feedback transfer function and performed analog solution of partial differential equations. The confocal feedback system was interfaced to a microcomputer via a laser scanner and video electronics to create a hybrid processor. Solutions to the three types of second-order partial differential equations in two dimensions (elliptic, hyperbolic, and parabolic) were obtained.

Based upon this work, it was determined that spherical aberrations in the CFPI resulted in a limited space-bandwidth product. An improved optical design using analysis by Johnston [14] attempted to increase the space-bandwidth product and the accuracy of the optical solution by introducing optical elements with spherical surfaces and negative lens effects into the simple confocal system. This analysis resulted in a Mangin mirror design which was experimentally evaluated by Fainman [9]. His results found that both the space-bandwidth product and the imaging characteristics of the CFPI using the Mangin mirrors were better than those obtained by using simple spherical mirrors.

Another problem with the CFPI was the optical losses introduced by scattering and absorption from any filters in the feedback. This had the effect of reducing the amount of feedback and reducing the effective number of iterations required to converge upon a solution. For this reason, emphasis was placed upon the development of a coherent image amplifier. Akins [1] used a dye laser and Rajbenbach [22] used two-beam coupling in $BaTiO_3$.

Typical uses for the CFPI have been as spectrum analyzers and etalons or resonators and laser cavities. Some research has looked into their use as spatial frequency filters. The use of the CFPI for optical processing is different in four ways:

(i) Input light enters off axis, off center, and only in one region of the input mirror.

(*ii*) The Fourier-transforming properties of the mirrors are used.

(*iii*) Spatial frequency image filters are inserted into the interferometer cavity.

(*iv*) A light amplifier can be placed into the cavity to compensate for losses.

The confocal feedback system used for this research and shown in Figure 4.1 is very similar to the one used by Lee and his co-workers. Lenses L_1 and L_2 image the input $a_i(x,y)$ telecentrically to the midplane C of the CFPI where it is coherently summed with a feedback signal to create $a_s(x,y)$. The optical amplifier amplifies $a_s(x,y)$ and the part of this light that is transmitted by M_2 constitutes the output $a_0(x,y)$ of the confocal system. The output is imaged from the midplane to a vidicon by L_3. The rest of the light is reflected into the feedback path where the spherical mirrors M_1 and M_2 function both as reflecting and Fourier-transforming elements. Mirror M_2 produces the Fourier transform $\tilde{a}_s(u,v)$ of $a_s(x,y)$ centered at point B in the midplane (u and v are the transform variables). Because the zero spatial frequency component of $a_s(x,y)$ propagates at an angle θ_{in} to the optical axis, point B is located a distance $r_m \theta_{in}/2$ above the optical axis, where r_m is the radius of curvature of the mirrors. $\tilde{a}_s(u,v)$ is spatially filtered by $\tilde{f}(u,v)$ at B and the result inverse-transformed by mirror M_1 to create $a_{fb}(x,y)$ which is filtered by $h(x,y)$. The transform of this signal then appears at point D and is spatially filtered by $\tilde{g}(u,v)$. Finally, the feedback image is inverse-transformed by M_1 and rejoins the original image with a phase shift β_{fb} which depends on the mirror separation.

This chapter will discuss adding the $BaTiO_3$ optical amplifier to a confocal feedback system designed to Lee's specifications. The goal will be to demonstrate the $BaTiO_3$ as an optical operational amplifier with the confocal feedback system providing negative feedback. Problems associated with the feedback phase control will be addressed so that the system can be kept from going into oscillation.

4-3
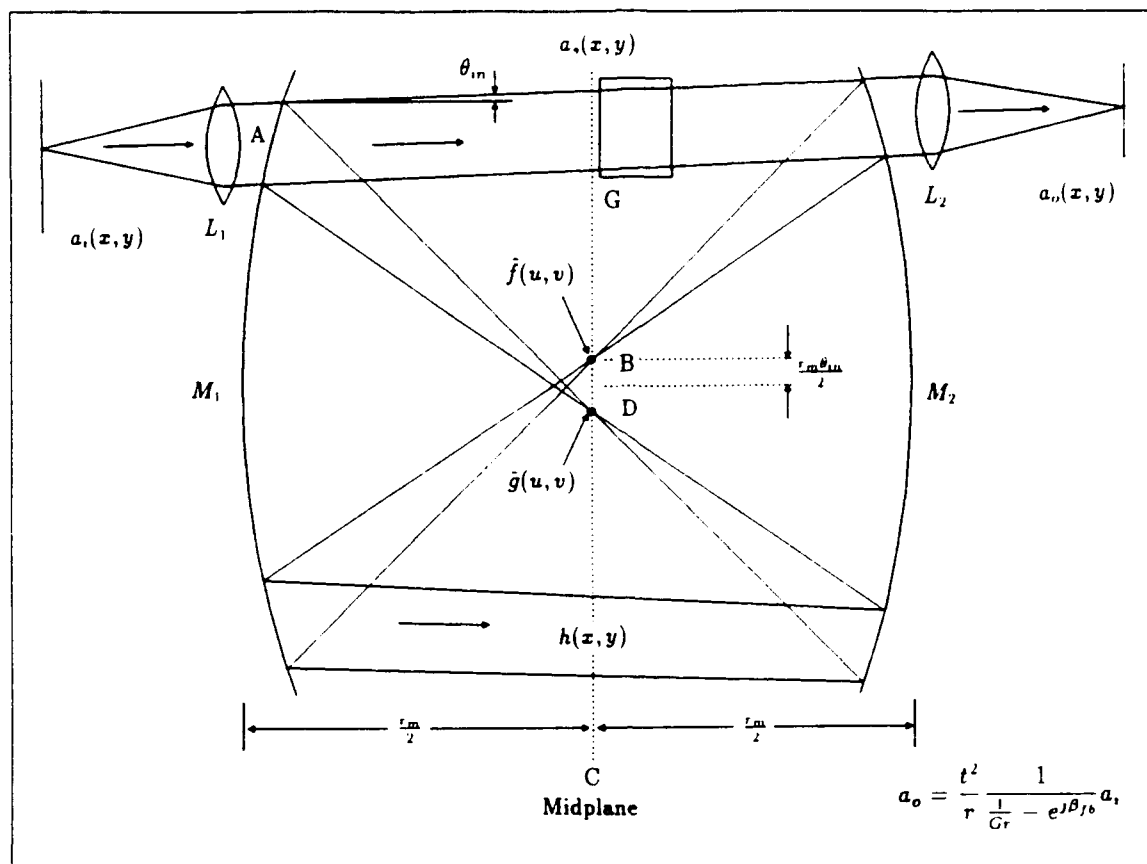
Figure 4.1. Confocal Feedback System

4.2 High Gain with Feedback

The transfer function for the $BaTiO_3$ amplifier in the confocal feedback system is developed in a manner similar to that of an operational amplifier with feedback. The output field is equal to the product of the transmission of the output mirror (t), the gain of the amplifier (G), and the field at the midplane (a_s) to give

$$a_o = tGa_s \tag{4.1}$$

The field at the midplane is the sum of the input field and the feedback field

$$a_s = ta_t + rGa_s e^{j\beta_{fb}} \tag{4.2}$$

where r is the round trip losses which includes mirror reflectivities, scattering losses, and transmission losses through the crystal or any other device in the beam. The

4-4

phase term β_{fb} represents the phase difference between the input and feedback optical waves. Solving these equations for the output field in terms of the input field results in

$$a_o = \frac{t^2}{r} \frac{1}{\frac{1}{Gr} - e^{j\beta_{fb}}} a_i \tag{4.3}$$

If the feedback phase is an even multiple of π then the system is unstable when $Gr \geq 1$. This condition represents a positive feedback system and when the gain becomes greater then, or equal to, the losses, oscillation occurs. This is how a ring laser works. On the other hand, if the feedback phase is an odd multiple of π, the system will be stable everywhere. This condition is equivalent to a negative feedback system. When $Gr \gg 1$ the transfer function of the system becomes linear, depending only upon the mirror transmissions and round trip losses. Even for small changes in the gain there will be little effect upon the system linearity, thus minimizing the effects of varying crystal gain.

4.3 Confocal Feedback System

The confocal feedback system used for these experiments is shown in Figure 4.2. The Mangin mirrors were built by IC Optical Systems LTD to specifications provided by Dr. Sing H. Lee at UCSD. The mirrors have a diameter of 72mm and are 15mm thick in the center. They are constructed from Heraeus Momosil glass with index of refraction 1.46181. The convex surface has a radius of 352.9mm and serves as the reflector with a split coating to give 98.5% and 94.0% reflectivity at 514.5 nm. The concave surface is antireflection coated for 514 nm and has a radius of curvature of 342.5mm. The effective focal length of each mirror is 35cm. One of the mirrors is mounted on a piezoelectric scanner for precision mirror spacing control. The $BaTiO_3$ crystal was placed in the midplane where the input light was imaged. Custom filters and a compensator for the crystal could be placed in midplane where the feedback path forms another image. Not shown in the figure is another laser beam path which is used to control the mirror spacing.
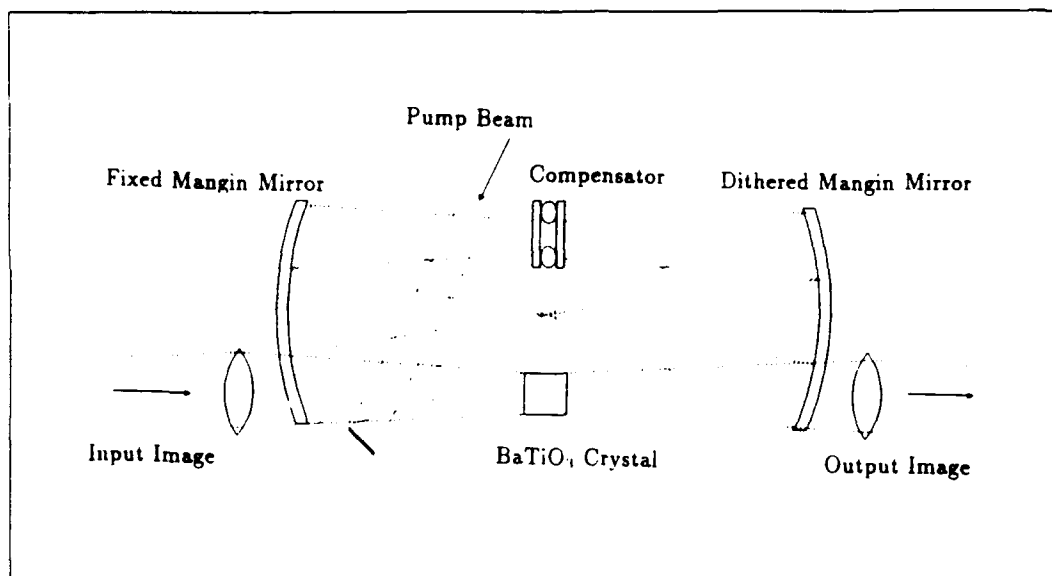
Figure 4.2. Mechanical Layout of Confocal Feedback System

The mirrors were aligned using the methods described by Wilson [30] and Hercher [13] and resulted in a central intensity fringe which was as large, or larger, than the mirror diameter. When there are no fringes the phase of the feedback is approximately uniform across the midplane within $\pm\pi/2$. The relationship between the diameter of this fringe (D) and the confocal feedback system space-bandwidth product is shown in Figure 4.3. The square boxes represent the areas in the midplane available for controlling the input information either in the image or Fourier domains. The outside dimension d of each box must then satisfy $d < D/4$ if there is no overlap between boxes and they must all stay within the central fringe. Information in the image having a resolution of n_x lines/mm will produce Fourier components spaced d_u apart where $d_u = 2.44\lambda n_x(r_m/2)$. The diameter of the central fringe was measured to be 36 mm thus d is 9mm and n_x can be no larger than 20 lines/mm. This would equate to 180 by 180 bits of information which could be used in the image plane and results in a space-bandwidth product of 32,400.

Since the mirror spacing is required to be constant while optical processing is being performed, an active control technique had to be incorporated using a piezo-
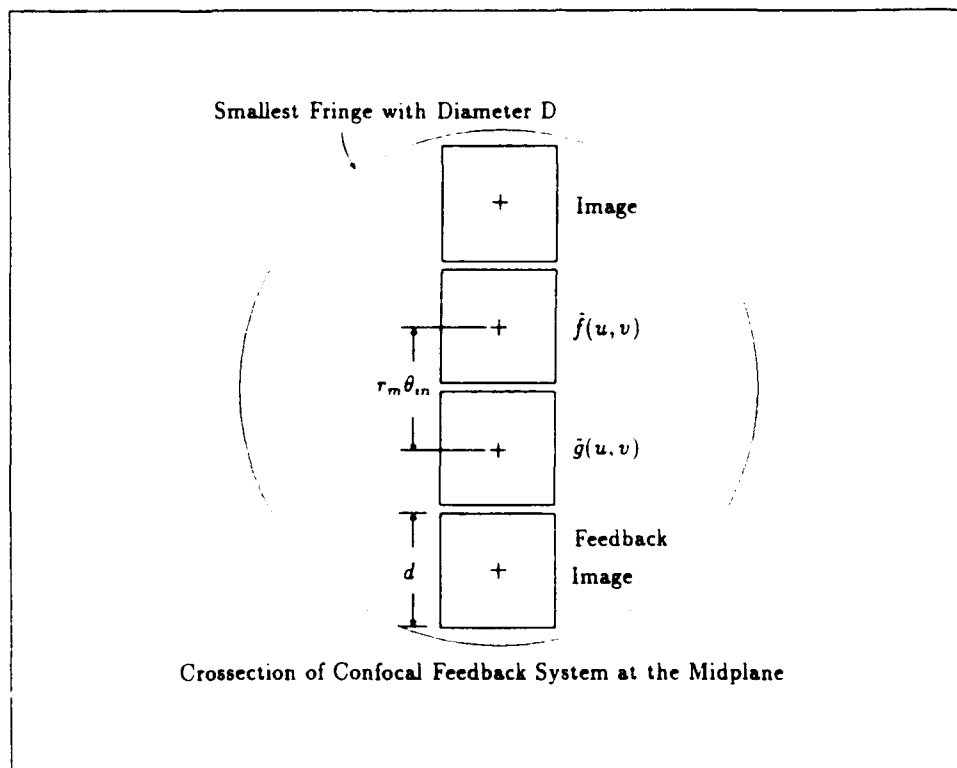
Figure 4.3. Relationship Between the Central Intensity Fringe and Confocal Feedback System Space-Bandwidth Product

electric compensator. A second laser beam is introduced into the confocal feedback system to provide a means for referencing the mirror spacing. A detector is then used to sense the peak intensity of reference beam light passing through the resonator. A Burleigh Fabry-Perot stabilization system/DAS-10 dithered the mirror spacing with a piezoelectric controller and provided a bias which kept the fringe on the detector and thus the mirror spacing constant. Using an expression derived by Hercher [13] the intensity interference patterns produced in the central plane of the interferometer are described by:

$$I(\rho) = \left(\frac{T_m}{1 - R_m^2}\right)\frac{I_o}{1 + (2F/\pi)^2 \sin^2(\delta/2)} \tag{4.4}$$

where ρ is fringe radius, T_m is the mirror transmission, R_m is the mirror reflectivity, I_o is the incident intensity, F is the finesse, and δ is the optical path difference in
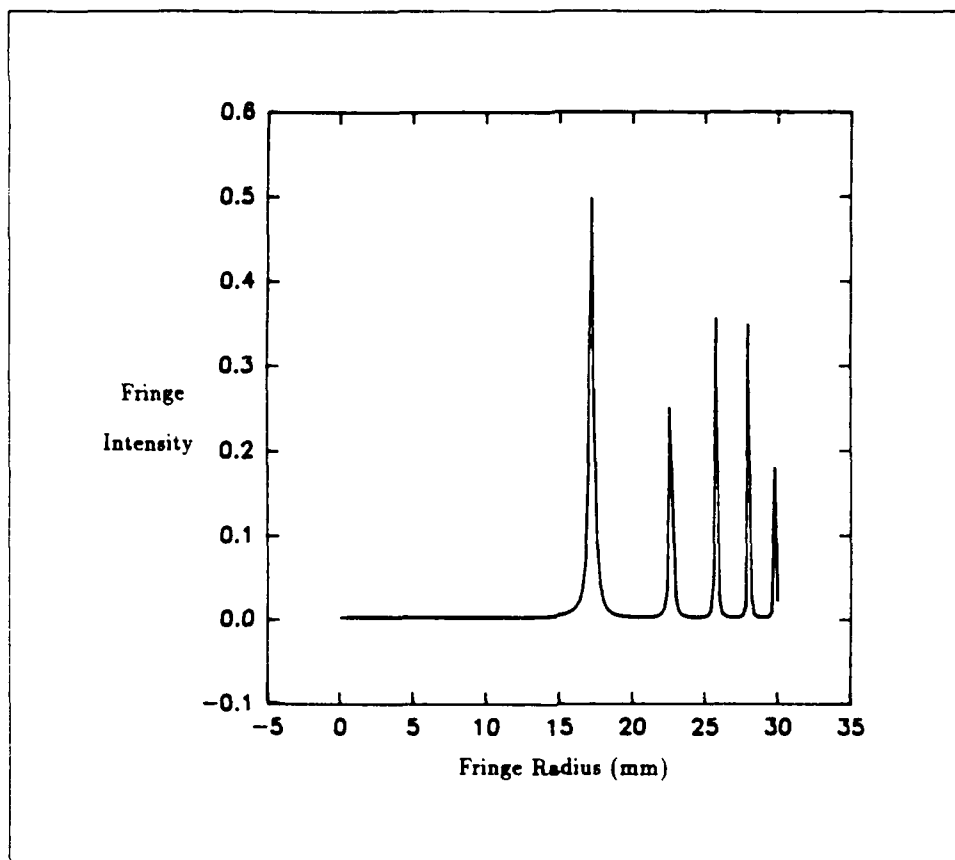
Figure 4.4. Fringe Intensity as a Function of Fringe Radius

radians. The finesse is given by

$$F = \frac{\pi R_m}{1 - R_m{}^2} \tag{4.5}$$

and the path difference is given by

$$\delta = \frac{2\pi}{\lambda}[\frac{\rho^4}{r_m{}^3} + 4\epsilon\frac{\rho^2}{r_m{}^2} + 4(r_m + \epsilon)] \tag{4.6}$$

where ϵ is the difference between the mirror spacing and the confocal spacing r_m.

Equation 4.4 is plotted in Figure 4.4 for three values of ϵ. This result figure graphically the results of Fainman [9] which recommends spacing the confocal mirrors slightly closer together than their common radius of curvature ($\epsilon < 0$) to get a larger area of constant phase in the midplane of the interferometer.

Another aspect of the fringes which is important is their sharpness, since this will determine how precisely the automatic stabilization system can control the phase of the feedback. The control system dithers the mirror spacing by some small amount around the peak of a fringe. By sensing and balancing the amplitudes of the fringe on either side of its peak, the system keeps the mirrors aligned to a constant spacing. A low finesse will give broad interference fringes and will result in a large variance in the optical feedback phase. The finesse for the mirrors used in this research is calculated to be 50 by assuming the split coating mirrors to have an effective reflectivity of 97%. The distance the moving mirror must travel to go between fringes $\triangle\epsilon_{f-f}$ is related to the motion required to go between the fringe's half power points $\triangle\epsilon_{1/2}$ is $\triangle\epsilon_{1/2} = \triangle\epsilon_{f-f}/F$. Thus, if the mirror controller were to dither the mirrors by $\triangle\epsilon_{1/2}$, the feedback phase angle will be dithered by $2\pi/F$. For a finesse of 50 this would equate to a phase error of $\pm 3.6°$. The actual ability to control the mirrors to this precision was not possible. The primary sources of error were instability of fringes due to air currents between the mirrors and the size of the detector as related to the fringe width which was required to provide a sufficient signal-to-noise. The accuracy of the operating system can be estimated from Figure 4.5 which displays fringe intensity as a function of relative mirror position. Based upon the photo, the fringes are 6 times the fringe width apart, resulting in an effective finesse of 6. Under these conditions the actual feedback phase was controlled to $\pm 60°$.

4.4 Frequency Stability Requirements

One of the requirements for using an optical amplifier with coherent feedback is that it be stable. If the phase of the feedback signal cannot be sufficiently controlled, negative feedback becomes positive feedback and the system goes into oscillation. On the surface this would not appear to be a problem with the BaTiO₃ optical amplifier using two-beam mixing. The optical bandwidth of the BaTiO₃ amplifier is on the order of a few hertz around the pump optical frequency while the longitudinal
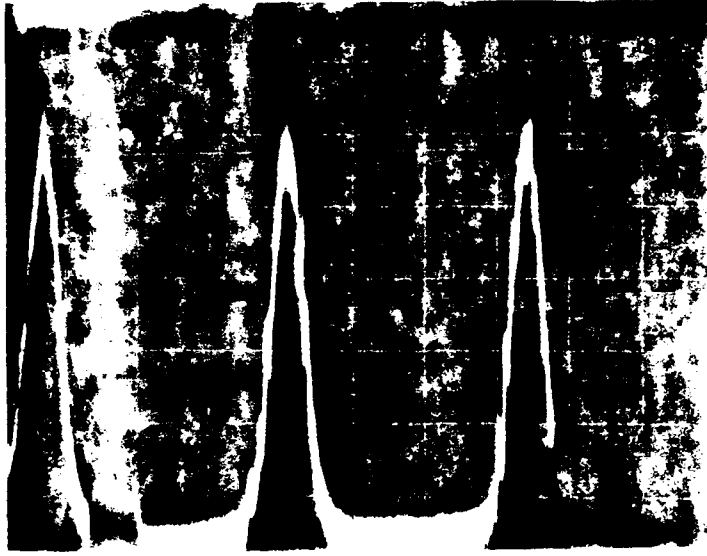
Figure 4.5. Fringe Intensity Resulting from Scanning the Mirrors

modes of the confocal system are separated by $c/(4r_m) = 1 \times 10^8 hz$. Controlling the confocal mirror spacing so that the phase of the optical feedback is an odd multiple of π has the effect of placing the pump laser frequency exactly halfway between the possible resonator modes. In spite of this, $BaTiO_3$ is famous for its ability to create oscillations in a ring laser configuration at almost any cavity length, provided that the two-beam coupling is strong enough [7, 36, 32]. The reason for this ability is due to a significant phase shift in the two-beam mixing output when the pump and signal optical frequencies are different.

The phase ψ in which the index grating is shifted spatially with respect to the light interference pattern can be found from the argument of $g(u)$ in Equation 2.29. For conditions in which $E_0 = 0$, $E_p \gg E_q$ (large θ), and $\tau_{di}/\tau_2 \ll E_p/E_q$ then

$$g(u) = \frac{-\triangle\omega + i}{1 + (\triangle\omega)^2} \tag{4.7}$$

$$\psi = \psi_0 + \tan^{-1}(\triangle\omega\tau_2) \tag{4.8}$$

where $\psi_0 = \pi/2$ for $BaTiO_3$. From this it can be seen that the phase of the grating will change depending upon the frequency difference between the pump and signal

4-10

beams' frequencies. Yeh [36] derived the following equation for the additional phase shift $\triangle\psi$ which is due to the photorefractive two-beam coupling.

$$\triangle\psi = -\frac{1}{2\tan\psi}ln(\frac{1+m_0^{-1}}{1+m_0^{-1}e^{-\gamma L}}) \qquad (4.9)$$

Using Equation 4.8, Equation 4.9 becomes

$$\triangle\psi = \frac{\triangle\omega\tau_2}{2}ln(\frac{(1+m_0)e^{\Gamma L}}{1+m_0e^{\Gamma L}}) \qquad (4.10)$$

where the imaginary part of Equation 4.7 is used to get

$$\Gamma = \frac{\Gamma_0}{1+(\triangle\omega\tau_2)^2} \qquad (4.11)$$

Γ is the same exponential gain coefficient as before and Γ_0 is the gain coefficient when $\omega_p = \omega_s$.

Figure 4.6 shows how $\triangle\psi$ varies as a function of $\triangle\omega\tau_2$. The input intensity ratio is chosen as a worst case where the input signal beam is the result of scattered light from the pump beam, thus $m_0 = 10^{-6}$. It can be seen that the crystal gain must be kept low enough so that the phase shift for all possible signal (noise) frequencies can be kept away from π and thus oscillation.

4.5 System Operation

The BaTiO$_3$ crystal is placed in the midplane where the input image is focused. Although it could be used anywhere in the confocal feedback loop, this is where the input light is in its most compact form and is the most controlled in terms of intensity and dynamic range. If the crystal is placed in one of the Fourier regions, the image amplification would be degraded since its spatial frequency components would not be amplified equally. Either the high intensity, low frequency components, would saturate or the high frequency, low intensity, components would not be amplified.

A problem is created with the high index crystal since it is not, in general, perfectly aligned so that its input face is perpendicular to the input light. Also, the
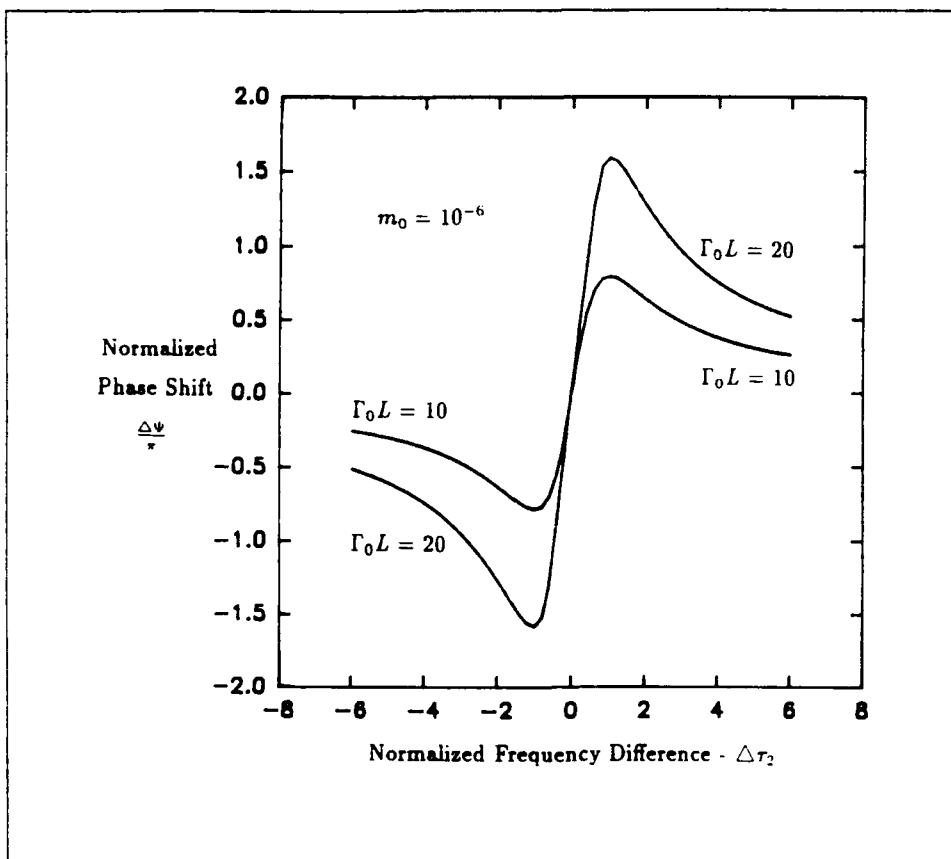
Figure 4.6. Photorefractive Phase Shift Due to Difference in Pump and Signal Frequencies

crystal's input and output faces are rarely perfectly parallel. When the crystal is positioned so that its faces are at an angle with respect to the incoming light, the light rays passing through the crystal will be translated from where they would have been if the crystal had not been there. This is shown in Figure 4.7. The problem is encountered when the light is reimaged onto the crystal after one round trip in the confocal system. The feedback image will be displaced by the same amount as it was when it left the crystal and does not overlap the original input signal. Successive round trips will continue to walk the beam off the crystal. The effect of this walk off is shown in Figure 4.8 in which a circular input beam is shown with successive round trips creating a slightly displaced image with each pass.
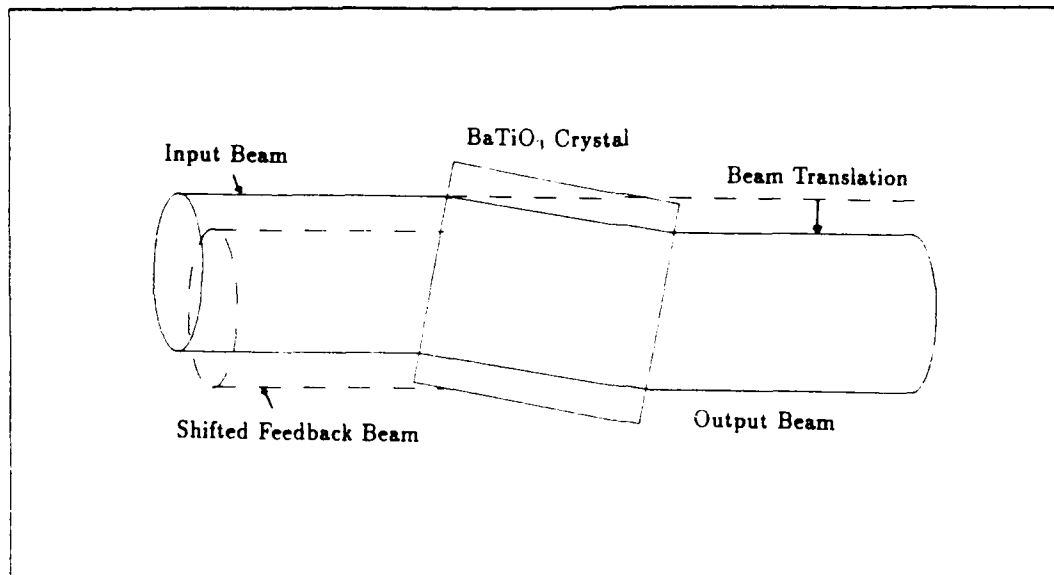
4-12

Figure 4.7. Beam Translation (Walk Off) Caused by Crystal Tilt

A similar problem is encountered by nonparallel crystal faces and is shown in Figure 4.9. The stable nature of the confocal system will assure that the feedback beam will be reimaged at the crystal face but it will be arriving from a slightly different direction. The Fourier transform of the image, however, will be displaced from its proper position and each successive round trip will result in additional displacement. The effect of this beam bending is shown in Figure 4.10. Since the feedback beam is reimaged on top of the input but at a slightly different angle, a series of interference fringes are created.

Both of these problems can be minimized by careful design and fabrication of the crystal and the immersion of the crystal into an index matching oil. This however does not lend itself to easy modification of the confocal system and spoils the ability to use available crystals. An alternate approach would be to insert a compensator into the image plane of the feedback path where it can be used to adjust for both beam translation and beam bending. This is approximately equivalent to using a crystal which is large enough to cover the entire midplane of the confocal system. The compensator, which was developed for this research, is shown in Figure 4.11
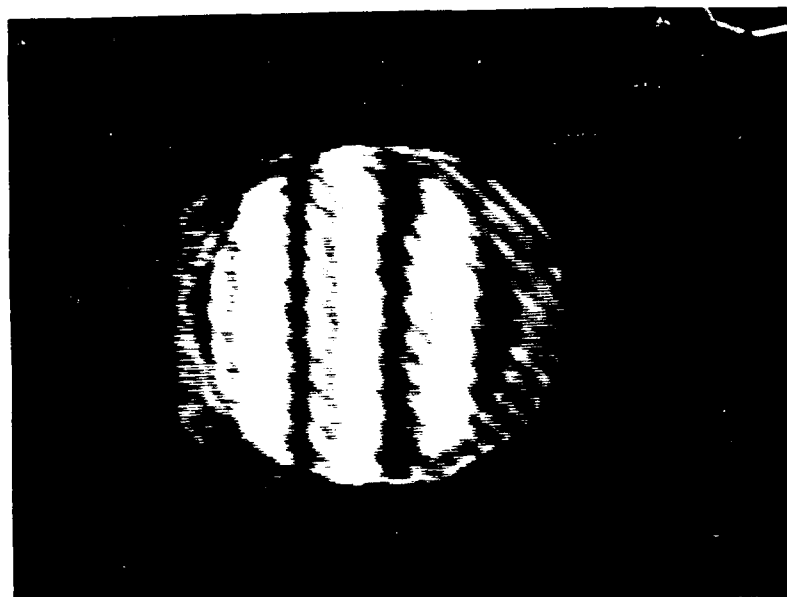
Figure 4.8. Image of Beam Translation (Walk Off) Caused by Crystal Tilt
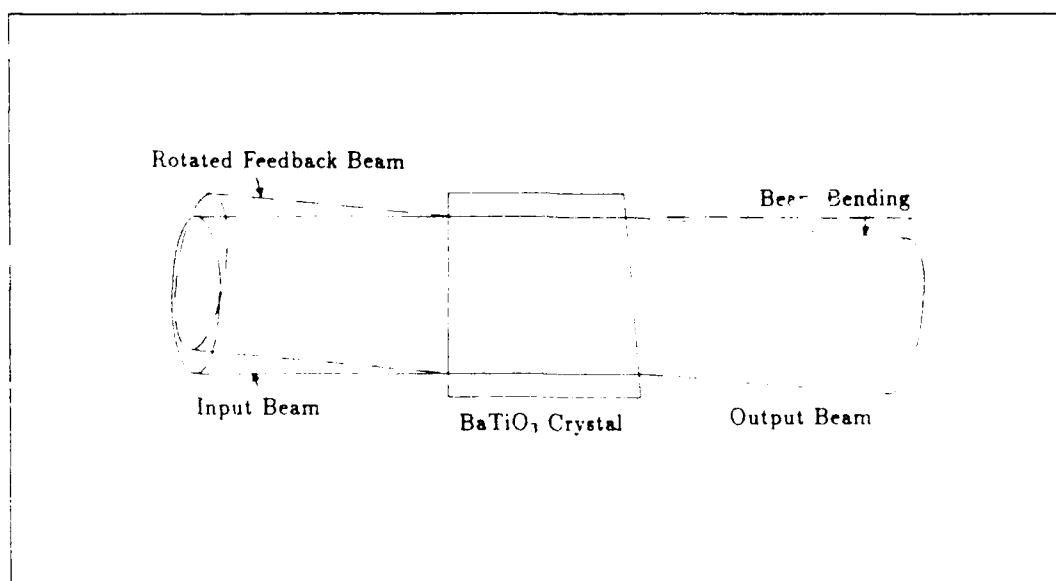

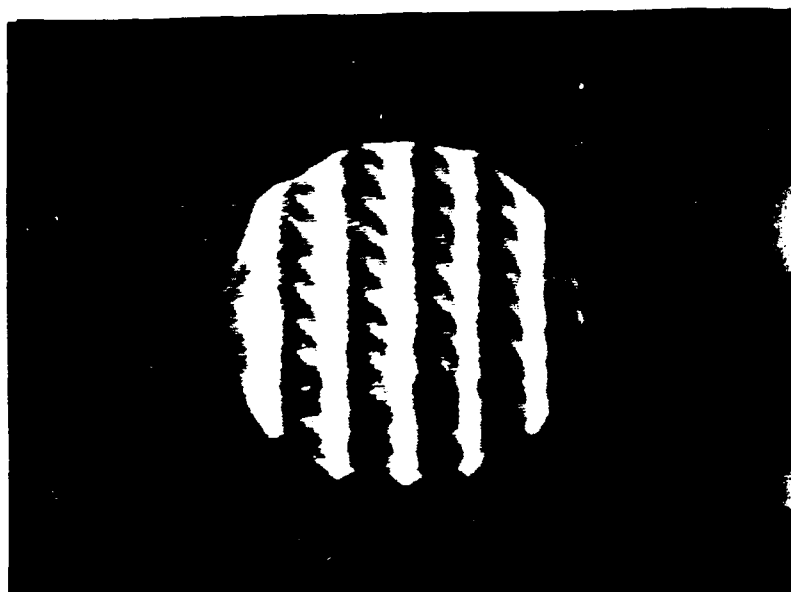Figure 4.9. Beam Bending Caused by Nonparallel Crystal Faces

Figure 4.10. Image of Beam Bending Caused by Nonparallel Crystal Faces

and is made from two pieces of bleached holographic plates sandwiching an index matching oil contained by an o-ring. When placed in the feedback path, beam translation can be corrected by rotating the compensator to create an equal and opposite effect. Likewise beam bending can be corrected by squeezing the o-ring in the proper manner to create an optical wedge which redirects the beam in the proper direction. Placement and adjustment of the compensator results in a midplane image with no walk off or fringes. A fully compensated image is shown in Figure 4.12. The fine fringes in this figure are the result of a filter in front of the TV camera and not the feedback system.

One final problem related to the $BaTiO_3$ crystal is the optical flatness of the faces. During the polishing process it is not uncommon for the faces to get rounded near the edges. This creates a nonuniform phase shift depending upon where the light passes through the crystal and could destroy the negative feedback criterion required to prevent oscillation. There is no easy correction for this problem other than having the faces repolished or imersing the crystal into an index oil to minimize the effect.
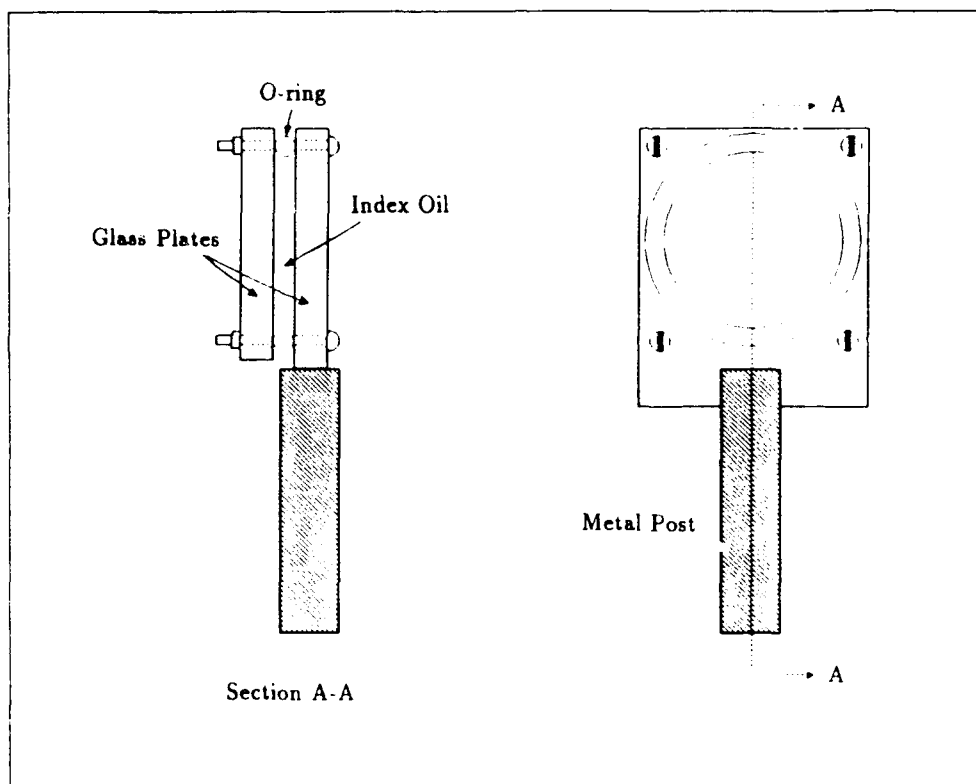
4-15

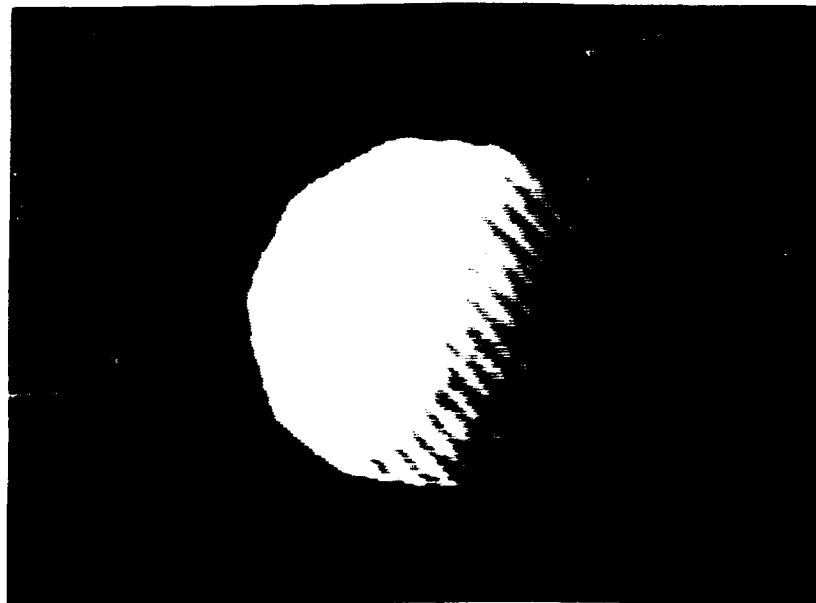Figure 4.11. Optical Feedback Compensator Design

Figure 4.12. Fully Compensated Feedback Image

1. AD	2. CODE										INDEXER	CATALOGER	EDITOR
A230532	FLD												
	GRP												
	SUB-GRP										REVIEWER	REVIEWER	VERIFIER

6. U-TITLE	11. DATE	16. PROJECT
7. C-TITLE	REGRADE DATE	17. TASK
8. T CLASS	12. RP	18. M-ACRONYM
9. DESC. NOTE	14. OA-SERIES	19. M-SERIES
10. AUTHOR	15. CONTRACT	20. R-CLASS

21. SUPPLEMENTARY NOTE

22. DISTRIBUTION/AVAILABILITY STATEMENTS

23. DESCRIPTORS

*

24. DESCRIPTOR CLASSIFICATION	U CRD	C CFRD	S SRD	R SFRD

25. IDENTIFIERS AND/OR OPEN-ENDED TERMS

26. IDENT. & O. E. TERMS CLASSIFICATION	U CRD	C CFRD	S SRD	R SFRD

27. ABSTRACT ☐ DTIC ☐ AUTHOR ☐ MOD. ☐ NO ABST.	28. ABSTRACT CLASSIFICATION	29. INVENTORY
☐ SEE BACK COPY FROM PAGE(S) _____	U CRD C CFRD S SRD R SFRD	1

30. INDEX ANNOTATION (MUST BE UNCLASSIFIED)

31. SPEC CODE	32. REGRADE CODE	33. DISTRIBUTION/ AVAILABILITY CODES	34. SERIAL NUMBER	36. DOCUMENT LOCATION
A X Y Z	A B C D E F G	DIST.	AVAIL. /SPECIAL	35. SOURCE CODE 012225	☐ 1 NTIS ☐ 2 DTIC

37. CLASS BY	38. DECLASS. ON	39. ... ON

Miror stabilization is accomplished by introducing a second beam into the feedback system. The second beam is required since the mirror control system requires a fringe peak in order to sense mirror spacing. Since negative feedback is required for the signal path, the signal is at a minimum and is not useable for mirror control. The best orientation for the reference beam is down the axis of the CFPI since there is no obstruction in this area and all other angles are blocked by a structure or optical element. Unfortunately the finess in this direction is no better than any other. Furthermore, since the input is symmetrical with the CFPI axis, a second set of fringes (first set - single pass, second set - double pass) further reduces the effective finess. The result of this poor finess is poor mirror control and an ustable feedback phase.

In operation, the feedback system is never sufficiently controlled to provide stable negative feedback. The crystal and input beams are first set to provide the maximum gain within the constraints of the fanning noise. The active control of the mirror spacing is then turned on and adjusted to produce a mirror spacing which results in a minimum signal beam image intensity. Unfortunately, due to the poor finess, the image is not completly dark ($180°$ feedback) since the mirrors have to be swept over such a large range to determine a peak in the reference beam fringe. When the pump beam is turned on, the system goes into oscillation. The problem of oscillation occurs for two reasons. The first is the inability to provide sufficient feedback phase control. The second is associated with the long and different signal and pump beam paths discussed earlier in Chapter III. The result is a low average signal beam gain and a high noise gain. Neither one of these problems can be readily fixed with the current setup.

4.6 Summary

The CFPI feedback system used for this research is not able to produce sufficient feedback phase control or signal beam gain to demonstrate the use of negative

feedback with a $BaTiO_3$ optical amplifier. Measurements and calculation of the spacing of interference fringes show the Mangin mirror design to be capable of providing a high space-bandwidth product. The system finess, however, is poor and results in unsatisfactory mirror spacing control for negative feedback. Calculations are made on the phase shift introduced by the $BaTiO_3$ crystal and a maximum gain criteria is established so that oscillation can be avoided. Practical problems are also addressed and solved in dealing with $BaTiO_3$ crystals which are not perfectly cut and aligned.

V. Conclusions and Recommendations

5.1 Conclusions

The objective of this dissertation was to analyze in detail the capabilities and limitations of using two-wave mixing in $BaTiO_3$ as an optical amplifier. Based upon the analysis, the gain was to be optimized within the constraints of amplified noise and desired dynamic range. Previous workers in this area had placed their emphasis upon optimizing gain and time response without considering the effect this optimizing had upon noise processes. The approach used in this dissertation was to theoretically analyze the two-beam gain process in detail so that all of the known parameters which affect it can be considered. The primary noise source was then analyzed in terms of the gain process so that the same gain parameters could also be used to minimize noise and optimize amplifier dynamic range. Measurements were then made to evaluate a $BaTiO_3$ crystal in an optimized configuration as a image amplifier and as an amplifier in a negative feedback configuration.

This work has resulted in four contributions to this area of technology. The first contribution is the development of a complete set of equations for two-beam gain in photorefractive crystals. These equations are unique in that the directional relationships between all of the parameters are maintained and there are no geometry assumptions buried in the derivation. The second contribution is the creation of a parameter for characterizing pump beam scatter (η_{scat}). Although researchers in the past few years have recognized that beam fanning is the result of amplified light scattered from the pump beam, no one has attempted to measure it or try to image it to better understand its nature. The third and most significant contribution, is the establishment of a procedure for optimizing amplifier gain and dynamic range. The key to this procedure is understanding how the gain available to both the signal and the noise can be controlled by the selection of the proper pump beam to c-axis angle. The dynamic range of an amplifier is determined by the pump beam

intensity, which represents the maximum output intensity, and the amplified noise, which represents the minimum output signal which can be observed. Since the noise source is a fixed fraction η_{scat} of the pump beam, increasing the gain will decrease the dynamic range. The selection of beam angles thus becomes a tradeoff between dynamic range and gain. The fourth contribution is the performance of an investigation into the development of an architecture for using the $BaTiO_3$ optical amplifier with negative feedback. A unique compensator was designed to correct for beam translation and deflection resulting from the crystal being tilted and having faces which are not parallel. Although the current system did not work, it is believed that with improvements an operational system could be developed. An architecture similar to this one, however, has been used in the development of an optical associative memory [3].

5.2 Recommendations

As a result of this research, the following recommendations are made:

1. A crystal of $BaTiO_3$ should not be cut to give a gain higher than necessary. Additional experiments should be performed with a $BaTiO_3$ crystal that is 1.5mm thick with faces cut $45°$ relative to the c-axis. With an internal pump-to-c-axis angle of $45°$ and an internal 2θ of $5°$, gains of 2×10^4 can be realized. If the scattering coefficient of the crystal is kept to 10^{-6}, a dynamic range of 100 (20 db) can be achieved. A thin crystal has the advantage of nearly complete overlap between the pump and signal beams thus assuring more crystal area for optical amplification and more efficient use of pump beam intensity. A thinner crystal will also have less absorption.

2. $BaTiO_3$ crystals which are to be used for optical amplification experiments should be antireflection coated. These coatings will improve the transmission of pump and signal beam transmission through the crystal and reduce the chances of producing an amplified double image.

3. Additional research needs to be performed into the sources of light scattering in photorefractive crystals. The reduction of scattered light from these sources will have a direct impact on improving the gain/dynamic range capabilities of a crystal.

4. Continued research into optical amplification with negative feedback needs to be performed. To accomplish this, additional work is required in designing a feedback technique for controlling the confocal Fabry Perot interferometer mirror spacing. Improvements to the optical compensator can also be made by making it smaller so that it blocks less of the midplane.

Bibliography

1. Akins, Robert P. and Sing H. Lee, "Two-Stage Injection-Locked Ring Dye Laser/Amplifier for Coherent Image Amplification," *Journal of the Optical Society of America A, 1*:533-536 (May 1984).

2. Ashkin, A. *et al.* "Optically Induced Index Inhomogeneities in $LiNbO_3$ and $LiTaO_3$," *Applied Physics Letters, 9*:72-74 (month? 1966).

3. Burns, Capt Thomas J. *A Compact Optical Associative Memory Using Dynamic Holographic Storage Media and Photorefractive Gain and Attenuation Elements*, MS Thesis, AFIT/GEO/ENG/90D-3, School of Engineering, Air Force Institute of Technology (AU), Wright-Patterson AFB OH, December 1990.

4. Cederquist, Jack and Sing H. Lee "The Use of Feedback in Optical Information Processing," *Applied Physics, 18*:311-319.

5. Cederquist, Jack and Sing H. Lee "Coherent Optical Feedback for the Analog Solution of Partial Differential Equations," *Journal of the Optical Society of America, 70*:944-953 (August 1980).

6. Ducharme, Stephen and Jack Feinberg. "Altering the Photorefractive Properties of $BaTiO_3$ by Reduction and Oxidation at 650 ° C, " *Journal of the Optical Society of America B, 3*:283-292 (February 1986).

7. Ewbank, M. D. and P. Yeh. "Frequency Shift and Cavity Length in Photorefractive Resonators," *Optics Letters, 10*:496-498 (October 1985).

8. Fainman, Y *et al.* "Optimal Coherent Image Amplification by Two-wave Coupling in Photorefractive $BaTiO_3$," *Optical Engineering, 25*:228-234 (February 1986).

9. Fainman, Y. and Sing H. Lee, "Experimental Evaluation of Mangin Mirror Performance for Optical Processing with Feedback," *Optical Engineering, 24*:535-540 (May/June 1985).

10. Feinberg, Jack *et al.* "Photorefractive Effects and Light-Induced Charge Migration in Barium Titanate," *Journal of Applied Physics, 51*:1297-1305 (1980); *52*:537 (1981).

11. Ford, Joseph E. *et al.* "Enhanced Photorefractive Performance from 45° -cut $BaTiO_3$," *Applied Optics, 28*:4808-4815 (November 1989).

12. Günter, P. "Holography, Coherent Light Amplification and Optical Phase Conjugation with Photorefractive Materials," *Physics Reports (Review Section of Physics Letters), 93*: 199-299 (1982).

13. Hercher, Michael "The Spherical Mirror Fabry-Perot Interferometer," *Applied Optics, 7*:951-966 (May 1968).

14. Johnston, Steve and Sing H. Lee, "Confocal Optical Feedback Processing System: An Improved Design," *Applied Optics, 22*:1431-1438 (May 1983).

15. Keppler, Capt Kenneth Scott. *Optical Amplification in 45°-cut BaTiO₃*, MS Thesis, AFIT/GEO/ENG/89D-5. School of Engineering, Air Force Institute of Technology (AU), Wright-Patterson AFB, OH, December 1987.

16. Klein, Marvin B. and R. N. Swartz. "Photorefractive Effect in BaTiO₃: Microscopic Origins," *Journal of the Optical Society of America B, 3*:292-305 (February 1986).

17. Kotljar, P. E. *et al. Optical Information Processing*, Vol. 2 (155-170). New York, Plenum Press, 1978.

18. Kukhtarev, N. V. *et al.* "Holographic Storage in Electrooptic Crystals. I. Steady State," *Ferroelectrics, 22*:949-960 (1979).

19. Kukhtarev, N. V. *et al.* "Holographic Storage in Electrooptic Crystals. II. Beam Coupling - Light Amplification," *Ferroelectrics, 22*:961-964 (1979).

20. Kukhtarev, N. V. *et al.* "Nonstationary Energy Exchange During Interaction Between Two Light Beams in Electrooptical Crystals", *Soviet Physics Technical Physics, 25*:1109-1114 (1980).

21. Nisenson, Peter and Sato Iwasa "Real-Time Optical Processing With $Bi_{12}SiO_{20}$ PROM," *Applied Optics, 11*:2760-2767 (December 1972).

22. Rajbenbach, Henre *et al.* "Optical Implementation of an Iterative Algorithm for Matrix Inversion," *Applied Optics, 26*: 1024-1031 (March 1987).

23. Rajbenbach, Henre *et al.* "Noise Suppression in Photorefractive Image Amplifiers," *Optics Letters, 14*:1274-1277 (Noveber 1998).

24. Rupp, R. A. and F. W. Drees. "Light-Induced Scattering in Photorefractive Crystals," *Applied Physics B, 39*:223-229 (1986).

25. Schunemann, P.G. *et al.* "The Effects of Feed Materials and Annealing Atmosphere on the properties of Photorefractive Barium Titanate Crystals," *Journal of the Optical Society of America B, 5*:1702-1710 (August 1988).

26. Schunemann, P.G. *et al.* "Role of Iron Centers in the Photorefractive Effect in Barium Titanate," *Journal of the Optical Society of America B, 5*:1685-1696 (August 1988).

27. Valley, George C. "Two-wave Mixing with an Applied Field and a Moving Grating," *Journal of the Optical Society of America B, 1*:868-873 (December 1984).

28. Valley, George C. "Competition Between Forward- and Backward-Stimulated Photorefractive Scattering in BaTiO₃," *Journal of the Optical Society of America B, 1*:868-873 (December 1984).

29. Vinetskii, V. L. *et al.* "Dynamic Self-diffraction of Coherent Light Beams," *Soviet Physics Usp, 22*:742-756 (1979).

30. Wilson, Capt Jeffery A. *Optical Information Processing in a Confocal Fabry-Perot Resonator*, MS Thesis, AFIT/GEO/ENG/88D-5, School of Engineering, Air Force Institute of Technology (AU), Wright-Patterson AFB OH, December 1988.

31. Yariv, Amnon and Pochi Yeh. *Optical Waves in Crystals*. New York: John Wiley & Sons, 1984.

32. Yariv, Amnon and Sze-Keung Kwong. "Theory of Laser Oscillation in Resonators with Photorefractive Gain," *Optics Letters, 10*:454-456 (September 1985).

33. Yeh, Pochi *et al.* "Photorefractive Nonlinear Optics and Optical Computing," *Optical Engineering, 28*:328-343 (April 1989).

34. Yeh,Pochi. "Photorefractive Two-Beam Coupling in Cubic Crystals, " *Journal of the Optical Society of America B, 4*: 1382-1386 (September 1987).

35. Yeh,Pochi. "Photorefractive Two-Beam Coupling in Cubic Crystals. II. General Case, " *Journal of the Optical Society of America B, 5*:1811-1813 (August 1988).

36. Yeh, Pochi. "Theory of Unidirectional Photorefractive Ring Oscillators," *Journal of the Optical Society of America B, 2*:1924-1928 (December 1985).

REPORT DOCUMENTATION PAGE

1. AGENCY USE ONLY (Leave blank)	2. REPORT DATE	3. REPORT TYPE AND DATES COVERED
	December 1990	Doctoral Dissertation

4. TITLE AND SUBTITLE

CHARACTERIZATION OF BARIUM TITANATE AS AN OPTICAL AMPLIFIER

5. FUNDING NUMBERS

6. AUTHOR(S)

George A. Vogel

7. PERFORMING ORGANIZATION NAME(S) AND ADDRESS(ES)

Air Force Institute of Technology, WPAFB OH 45433-6543

8. PERFORMING ORGANIZATION REPORT NUMBER

AFIT/DS/ENG/90D-3

9. SPONSORING/MONITORING AGENCY NAME(S) AND ADDRESS(ES)

10. SPONSORING/MONITORING AGENCY REPORT NUMBER

11. SUPPLEMENTARY NOTES

12a. DISTRIBUTION/AVAILABILITY STATEMENT

Approved for public release; distribution unlimited

12b. DISTRIBUTION CODE

13. ABSTRACT (Maximum 200 words)

The introduction of two-beam coupling in photorefractive materials has resulted in an extensive amount of research into their use as optical processing/computing elements. This dissertation develops the theoretical equations for two-beam coupling in barium titanate and applies them to develop a specification which optimizes barium titanate as an optical amplifier.

One of the factors which limits the optical gain in photorefractive crystals is the loss of pump beam power to the amplification of parasitic light (beam fanning). This parasitic light is produced by light scattered from the pump beam by imperfections on both the crystal face and within the crystal. Through the analysis of signal and noise amplification as functions of pump and signal beam angles relative to the crystal c-axis, an optimum pump angle is defined which maximizes signal gain and minimizes the energy lost to beam fanning. The determination of an optimum gain is based upon a desired dynamic range and the crystal scattering characteristics.

A potential application for the barium titanate optical amplifier is investigated in a system which produces negative feedback using destructive interference. Applications for such a system include image restoration, linear amplification, and image filtering.

14. SUBJECT TERMS

barium titanate, photorefractive, two-beam coupling, optical amplifier, holography, optical feedback

15. NUMBER OF PAGES

92

16. PRICE CODE

17. SECURITY CLASSIFICATION OF REPORT	18. SECURITY CLASSIFICATION OF THIS PAGE	19. SECURITY CLASSIFICATION OF ABSTRACT	20. LIMITATION OF ABSTRACT
Unclassified	Unclassified	Unclassified	UL

Vita

George A. Vogel ████████████████████████████████ He graduated from Xenia High School in Xenia, Ohio in 1967 and attended the University of Cincinnati, graduating with a Bachelor of Science in Electrical Engineering in June 1972. From graduation to the present he has worked as a Project Engineer in the Electronic Warfare Division of the Avionics Laboratory at Wright-Patterson AFB, Ohio. During this period he has specialized in the areas of optical and infrared countermeasures and manages an in-house infrared missile simulation facility. In June 1976 he began part time study at the Air Force Institute of Technology and completed the program in June 1981 with a Masters of Science in Engineering Physics. As part of this program he performed research which resulted in a thesis entitled *Analysis of XeCl Emission in a Hollow Cathode Discharge*. He was admitted to candidacy for the degree of Doctor of Philosophy in the School of Engineering, Air Force Institute of Technology, in June 1986.